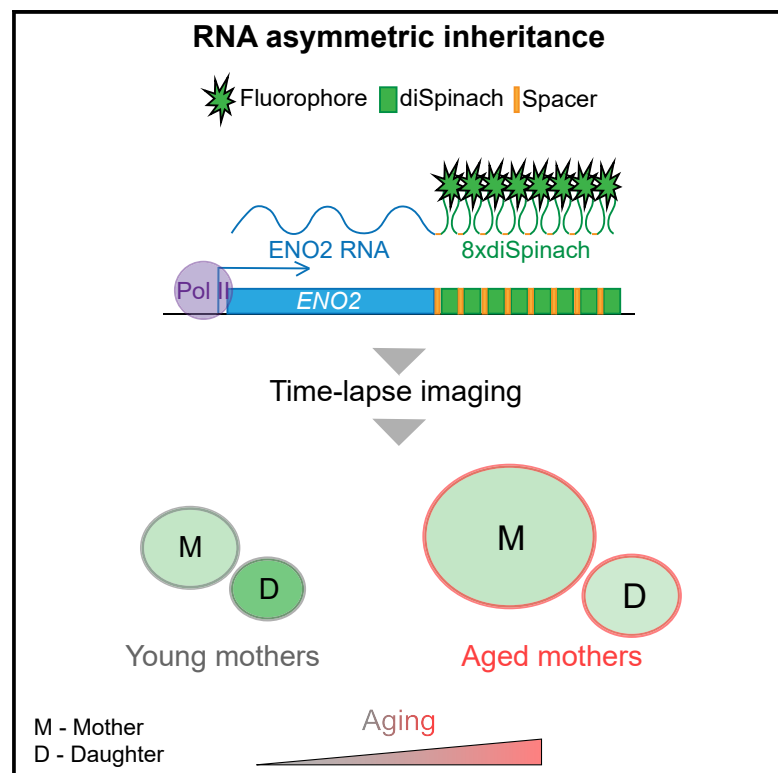# Quantitative RNA imaging in single live cells reveals age-dependent asymmetric inheritance

Graphical abstract

Highlights

- diSpinach aptamer tagging to study RNA inheritance in cells on a microfluidics device

- ENO2 RNA, visualized through diSpinach, is asymmetrically distributed to daughters

- Loss of asymmetric RNA inheritance is a direct consequence of cellular aging

- Sir2 is essential for the asymmetric RNA inheritance

Authors

Igor V. Kukhtevich,
Mariana Rivero-Romano,
Namisha Rakesh, ..., Antonis Kirmizis,
Kurt M. Schmoller, Robert Schneider

Correspondence

robert.schneider@helmholtz-muenchen.de

In brief

Kukhtevich et al. propose an approach to quantify RNA dynamics in single cells across several generations in a microfluidics device by tagging RNAs with the diSpinach aptamer. The results suggest that, in *S. cerevisiae*, ENO2 diSpinach RNA is inherited asymmetrically by daughters and that this is an aging-dependent phenomenon.

CelPress

Cell Reports

Resource

Quantitative RNA imaging in single live cells reveals age-dependent asymmetric inheritance

Igor V. Kukhtevich,[1] Mariana Rivero-Romano,[1,2] Namisha Rakesh,[1,3] Poonam Bheda,[1] Yagya Chadha,[1] Paulina Rosales-Becerra,[2] Stephan Hamperl,[4] Daniela Bureik,[1] Scarlett Dornauer,[1] Catherine Dargemont,[5] Antonis Kirmizis,[6] Kurt M. Schmoller,[1] and Robert Schneider[1,3,7,*]

[1]Institute of Functional Epigenetics, Helmholtz Zentrum München, 85764 Neuherberg, Germany
[2]Instituto de Biotecnologia, National Autonomous University of Mexico, Cuernavaca 62210, Mexico
[3]Faculty of Biology, Ludwig-Maximilians-Universität München, 82152 Planegg-Martinsried, Germany
[4]Institute of Epigenetics and Stem Cells, Helmholtz Zentrum München, 81377 Munich, Germany
[5]Institute of Human Genetics, UMR 9002 CNRS – University of Montpellier, 34094 Montpellier Cedex, France
[6]Department of Biological Sciences, University of Cyprus, 1678 Nicosia, Cyprus
[7]Lead contact
*Correspondence: robert.schneider@helmholtz-muenchen.de
https://doi.org/10.1016/j.celrep.2022.111656

SUMMARY

Asymmetric inheritance of cellular content through cell division plays an important role in cell viability and fitness. The dynamics of RNA segregation are so far largely unaddressed. This is partly due to a lack of approaches to follow RNAs over multiple cellular divisions. Here, we establish an approach to quantify RNA dynamics in single cells across several generations in a microfluidics device by tagging RNAs with the diSpinach aptamer. Using *S. cerevisiae* as a model, we quantitatively characterize intracellular RNA transport from mothers into their buds. Our results suggest that, at cytokinesis, ENO2 diSpinach RNA is preferentially distributed to daughters. This asymmetric RNA segregation depends on the lifespan regulator Sir2 and decreases with increasing replicative age of mothers but does not result from increasing cell size during aging. Overall, our approach opens more opportunities to study RNA dynamics and inheritance in live budding yeast at the single-cell level.

INTRODUCTION

During the cell cycle, many cellular components have to be duplicated. At cell division, the content of cells is distributed between the progenies to ensure that both cells inherit all components necessary for cell viability and adaptation. In some cases, this segregation of cellular components is not equal, either because of stochastic distribution or active transport, with both resulting in different states of the sister cells (Müller et al., 2007; Chernova et al., 2014; Zion et al., 2020). This asymmetric inheritance of cellular content can play a key role in cell viability, cell differentiation, adaptation to changing environments, and evolutionary fitness and fulfills critical functions during the development of multicellular organisms (Lerit et al., 2013; Moore and Jessberger, 2017; Shlyakhtina et al., 2019).

In the budding yeast *S. cerevisiae*, asymmetric inheritance of cellular components is crucial for replicative aging and rejuvenation of daughter cells in budding yeast (Shlyakhtina et al., 2019). For example, aggregates of damaged proteins (Chernova et al., 2014) as well as extrachromosomal ribosomal DNA circles (Shcheprova et al., 2008; Denoth-Lippuner et al., 2014) are asymmetrically accumulated in mother cells, contributing to mother aging and supporting daughter cell rejuvenation. Thus, although the implication of this asymmetric inheritance of cellular

components on replicative aging is relatively well studied, little is known about the effect of replicative aging on asymmetric inheritance.

Our knowledge about the asymmetric distribution of organelles and proteins heavily relies on use of fluorescent fusion proteins, which enable us to follow the asymmetric distribution in single cells using live-cell microscopy. However, these approaches cannot be transferred to study the dynamics and inheritance of RNA in single cells.

Several fluorescence microscopy-based methods have been described to measure RNA levels in single live cells (Bratu et al., 2003; Tyagi, 2007, 2009; Ozawa et al., 2007; Urbanek et al., 2014; Lenstra and Larson, 2016), including fluorescently tagged RNA binding proteins (coat proteins) that recognize specific RNA motifs, such as MS2 (Tyagi, 2007) or PP7 (Lenstra and Larson, 2016), inserted into RNAs. Recently, "light-up" RNA aptamers that specifically bind to an externally supplied fluorophore have emerged as a promising alternative (Bouhedda et al., 2018). Examples include the Spinach and Mango aptamers, as well as their derivatives iSpinach and Mango III (Paige et al., 2011; Autour et al., 2016, 2018; Dolgosheina et al., 2014; Panchapakesan et al., 2017), which bind the fluorophores 3,5-difluoro-4-hydroxybenzylidene imidazolinone (DFHBI), DFHBI-1T, or thiazole orange-biotin fluorophore complexes (TO1-biotin and

A

Time-lapse single-cell imaging

RNA inheritance

B

D

C

2μOri plasmid with *ACT1pr-mCHERRY-NxdiSPINACH*

(legend on next page)

TO3-biotin), respectively. In *S. cerevisiae*, the Spinach aptamer has been introduced into the galactose-inducible *GAL1* gene as well as *STL1* and *ASH1* without significantly modifying the function of the tagged transcripts (Guet et al., 2015), but microscopy analysis was limited to less than 20 min.

Here we study the inheritance of RNA from mother to daughter cells at the single-cell level over multiple generations. We established an approach to image and quantify highly and moderately expressed RNAs in live yeast cells. We combined tagging of RNA with the light-up RNA aptamer diSpinach with a custom-made microfluidics device that enables parallel long-term imaging of multiple yeast strains over many generations. This approach can be used to simultaneously quantify RNA and protein levels in single cells over time. We were able to quantitatively track RNA transport from mother cells into their buds with high temporal resolution. As a model, we tagged ENO2 RNA with 8×diSpinach and identified a preferential distribution of transcripts to daughter cells. During replicative aging, the asymmetric distribution of the diSpinach signal between daughters and mothers is lost. We show that this effect is not simply due to the increase in cell size associated with aging but a direct consequence of aging and that it is dependent on the longevity factor Sir2.

RESULTS

The RNA aptamer diSpinach can be used for RNA imaging in live yeast cells

To explore whether light-up aptamers are suitable for live-cell RNA imaging and for following RNA inheritance throughout cell division in budding yeast, we tested the RNA aptamer diSpinach (Figure S1) as well as the previously reported aptamer Mango III (Autour et al., 2018). diSpinach is a dimeric derivative of the iSpinach aptamer (Autour et al., 2016), which combines the decreased salt sensitivity and thermal stability of iSpinach with increased fluorescence intensity. To improve the folding efficiency of iSpinach and its interaction with DFHBI-1T, two repeats of the iSpinach aptamer were combined without any linker (Figure S1A). We first tagged the RNA of the reporter mCherry encoded on a 2μOri high-copy plasmid under control of the strong *ACT1* promoter with four repeats of *diSPINACH* or 12 repeats of *MANGO III*. This construct allows simultaneous detection of the protein signal corresponding to the tagged RNA because of expression of the reporter mCherry. We opted for multiple aptamer repeats because use of single copies of the original Spinach aptamer results in no or very low RNA signals (Zhang et al., 2015). To minimize interference with the

RNA, we initially chose 4 repeats of diSpinach and 12 for Mango III so that the total length is around half of that of most fluorescent protein tags used for live-cell imaging of proteins.

We imaged exponentially growing cells with DFHBI-1T or TO1-B, the fluorophores binding diSpinach or Mango III, respectively (STAR Methods). For mCHERRY RNA tagged with 4×diSpinach, we observed a clear RNA signal above the control (Figure S2A) and noticed that cells with a strong mCherry signal also showed bright fluorescent foci and overall increased fluorescence in the diSpinach channel. This suggests a direct correlation between protein and RNA signal strengths. In contrast, for 12×Mango III we detected no signal above the control even though the corresponding protein signal was detected (Figure S2B). Deletion of the transporter *PDR5* did not increase Mango III-associated RNA signals (Figure S2B), suggesting that the lack of signals is not due to export of TO1-B from the cells by multidrug transporters (Ernst et al., 2005). Thus, we conclude that diSpinach is more promising for live-cell RNA imaging in *S. cerevisiae*.

Development of a microfluidics device for live single-cell imaging and optimization of diSpinach repeat number

For long-term single-cell imaging under defined conditions, we designed and manufactured a custom-made microfluidics device that allows medium exchange with a wide range of flow rates (STAR Methods), making it suitable for imaging RNA aptamers. Briefly, this device consists of 8 separate chambers, each with 10 regions for single-cell imaging; is easily adaptable to any commercial microscope (Figure 1A); and can be used for simultaneous imaging of 8 strains.

We first applied the microfluidics device to optimize the number of diSpinach repeats needed to detect RNAs with varying levels of expression. For this, we compared strains transformed with 2μOri expression plasmids encoding *ACT1pr-mCHERRY* fused to 1×, 2×, 4×, 8×, or 16× repeats of *diSPINACH* (Figure 1B). the length of 8×diSpinach (1,100 bp) is comparable with the length of commonly used fluorescent protein tags. Variation in copy number of 2μOri expression plasmids from a few to ~100 copies per cell (Zakian et al., 1979) (e.g., because of unequal transmission of the plasmid to buds) gives access to a wide range of different RNA expression levels. Even in cells with relatively high mCherry expression, the signal for the 1×diSpinach tag (Figure 1C) yields only very weak fluorescence, close to the autofluorescence observed for the

Figure 1. Pipeline for imaging and analyzing tagged RNA in single live cells

(A) Left: custom-made microfluidics device with 8 chambers for live-cell imaging. In each chamber, one yeast strain can be loaded and grown in the focal plane for many hours (see magnification). Each chamber contains 10 regions with 3-μm height for single-cell isolation. Center: representative images of a time-lapse experiment at 0 and 10 h. Right: schematic summary of the image analysis (for more details, see Figure S2E).

(B) Schematic of RNA tagging with different numbers of diSpinach repeats.

(C) Comparison of representative images acquired in the indicated channels for yeast transformed with 2μOri plasmids containing *ACT1pr-mCHERRY-1/2/4/8/16×diSPINACH* and non-transformed cells as an autofluorescence control. Cells were grown in the custom microfluidics device in SCD with 50 μM DFHBI-1T. All images were acquired using the same settings. 10 h of imaging.

(D) Mean RNA (diSpinach) signal for cells with corresponding protein (mCherry) intensity values of 500, 1,000, 2,000, 4,000, and 8,000 (a.u.) (averaged across ±100 [a.u.] bins, N ≤ 746 cells for each bin). Note the increase in RNA signal with increasing diSpinach repeat number for cells with similar protein signals. Standard errors are smaller than 67 [a.u.] and, thus, not visible. Dashed line, median fluorescent intensity in control cells plus two standard deviations.

Mothers and buds were counted as separate cells starting from bud emergence. See also Figures S1, S2, and S3.

non-transformed control. In contrast, the 8×diSpinach and 16×diSpinach tags resulted in a robust fluorescence signal, enabling visualization of RNAs even in cells with relatively weak mCherry fluorescence. Although northern blot analysis with *mCHERRY* as a probe confirmed the presence of one major RNA species corresponding to the expected full-length RNAs (Figure S1C), using a probe against *diSPINACH* suggests the additional presence of potential RNA cleavage or decay products (Figure S1D) that do not contain the mCHERRY coding part.

To quantify RNA and protein signals, we used a 5 × 5 pixel moving average filter approach to distinguish fluorescence signals from noise and corrected for the background signal (Figures 1A, S2D, and S2E). We applied a semiautomatic pipeline for segmenting cell contours based on the phase-contrast images using Phylocell (Fehrmann et al., 2013). For each strain, we pooled the data for all analyzed cells at all time points and compared the mean RNA signals with the mean protein signals (Figures 1D and S1B). In agreement with our visual inspection (Figure 1C), the 1×diSpinach tag displayed fluorescence intensity values close to those in control cells. An increased number of diSpinach repeats allows visualization of RNAs in cells with medium (4×diSpinach) and even low mCherry signal (8×diSpinach and 16×diSpinach). The 16×diSpinach tag resulted in a stronger signal than the 8×diSpinach tag but led to an increased number of cells with enlarged cell size and a delay in cell cycle progression. Therefore, we conclude that the 8×diSpinach tag is best suited for live-cell imaging of RNAs with a wide range of expression levels.

Analysis of RNA and protein levels in single cells over an extended time

We next validated our approach for long-term imaging by correlating RNA and protein levels in single cells over an extended time. For this, we imaged cells transformed with *ACT1pr-mCHERRY-8×diSPINACH* on a 2μOri plasmid for 10 h (Figure S3). To reliably distinguish RNA-dependent signals from autofluorescence in individual cells, we refined our analysis pipeline, which we called the "quantitative approach." We counted, for each cell at each time point, the number of pixels with signal intensity above a threshold, set as median plus two standard deviations of the signal intensities observed in control cells (Figures S2E and S2F). For cells with more than 5 pixels above this threshold, we summed the intensity of all of those pixels (after background subtraction) and normalized this total intensity by cell area. In line with our initial observations, this quantitative approach revealed a strong correlation between the intensity values for diSpinach (RNA) and mCherry (protein) signals across all cells pooled together independent of cell history (Pearson $R = 0.84$, $p < 10^{-30}$; Figure 2A). Next we wanted to determine whether this correlation is mainly due to inter-cell variability of, e.g., plasmid copy number or also due to correlated changes in protein and RNA levels in individual cells over time. We therefore first compared mCherry signal with and without the 8×diSpinach tag (Figures S4A and S4B), confirming a similar range of signals. Then we tracked 27 cells with different mCherry expression levels and calculated correlation coefficients between RNA and protein

signals within single-cell traces (Figure 2B). We found that protein and RNA levels were correlated over time (median Pearson correlation coefficient $R = 0.62$, $p < 10^{-21}$). This demonstrates that our pipeline can be used to detect and follow RNA in single cells for at least 10 h.

The 8×diSpinach tag could be used for imaging endogenous coding and non-coding RNAs

Next we used diSpinach to visualize transcripts with different expression levels over time. For highly expressed genes, we endogenously tagged *ENO2*, encoding for the phosphopyruvate hydratase enolase II, and *HTB2* (Miura et al., 2008), encoding for histone H2B, with *8×diSPINACH*. As an example of low expression levels, we chose the *HHO1* promoter, which produces only a few transcripts per cell (Nadal-Ribelles et al., 2019; Miura et al., 2008), and integrated an *HHO1pr-mCHERRY-8×diSPINACH*-containing plasmid as a single copy into the *URA3* locus. Visual inspection revealed clear diSpinach signals for *ENO2*, *HTB2*, as well as the *HHO1* promoter-driven transcripts (Figure S3). By applying our quantitative analysis approach, we found that the mean diSpinach signal intensities obtained for *ENO2* and *HTB2* transcripts were significantly higher than for the control (Figure 2C). In agreement with previous studies, the mean ENO2 diSpinach signal was stronger than the mean HTB2 diSpinach signal (Nadal-Ribelles et al., 2019; Miura et al., 2008; Figure 2C). However, the mean fluorescence values observed for *HHO1* promoter-driven expression were not significantly different from the control (Figure 2C). This may be due to weak expression and because the intensity values we obtained might be dominated by cells with no *HHO1* transcriptional activity; for example, because of cell cycle-dependent expression.

To investigate this further, we introduced an alternative quantification pipeline for which we determined the fraction of cells with RNA signal above a threshold (Figures S2E and S2F). Using this "binary" approach, we found that, for *ENO2*, practically all cells (99%) showed detectable diSpinach signal. In contrast, for *HTB2* and *HHO1* promoter-driven expression, only a small but significant subpopulation of cells (10.4% and 17.2%, respectively) displayed fluorescence RNA signals above the selected threshold (Figure 2D).

Next we wanted to explore whether this low percentage of expressing cells is due to cell cycle-dependent expression of *HTB2* and of the transcript generated from the *HHO1* promoter. We thus tracked cells over time, aligned them at the time of bud emergence, and calculated the mean diSpinach signal as a function of time throughout the cell cycle as well as the number of cells with detectable diSpinach signal. As expected (Spellman et al., 1998), we found that the signals from endogenously tagged *ENO2-8×diSPINACH* and *ACT1pr-mCHERRY-8×diSPINACH* expressed from a 2μOri plasmid are largely cell cycle independent (Figure 3A) and that RNA signals are present in nearly all cells (Figure 3B). In contrast, for HTB2, the diSpinach signal and the fraction of cells with diSpinach signal reach a maximum around the time of bud emergence, which corresponds to the beginning of S phase (Figures 3C and 3D). Similarly, using the binary approach, we observed a clear cell cycle dependence for
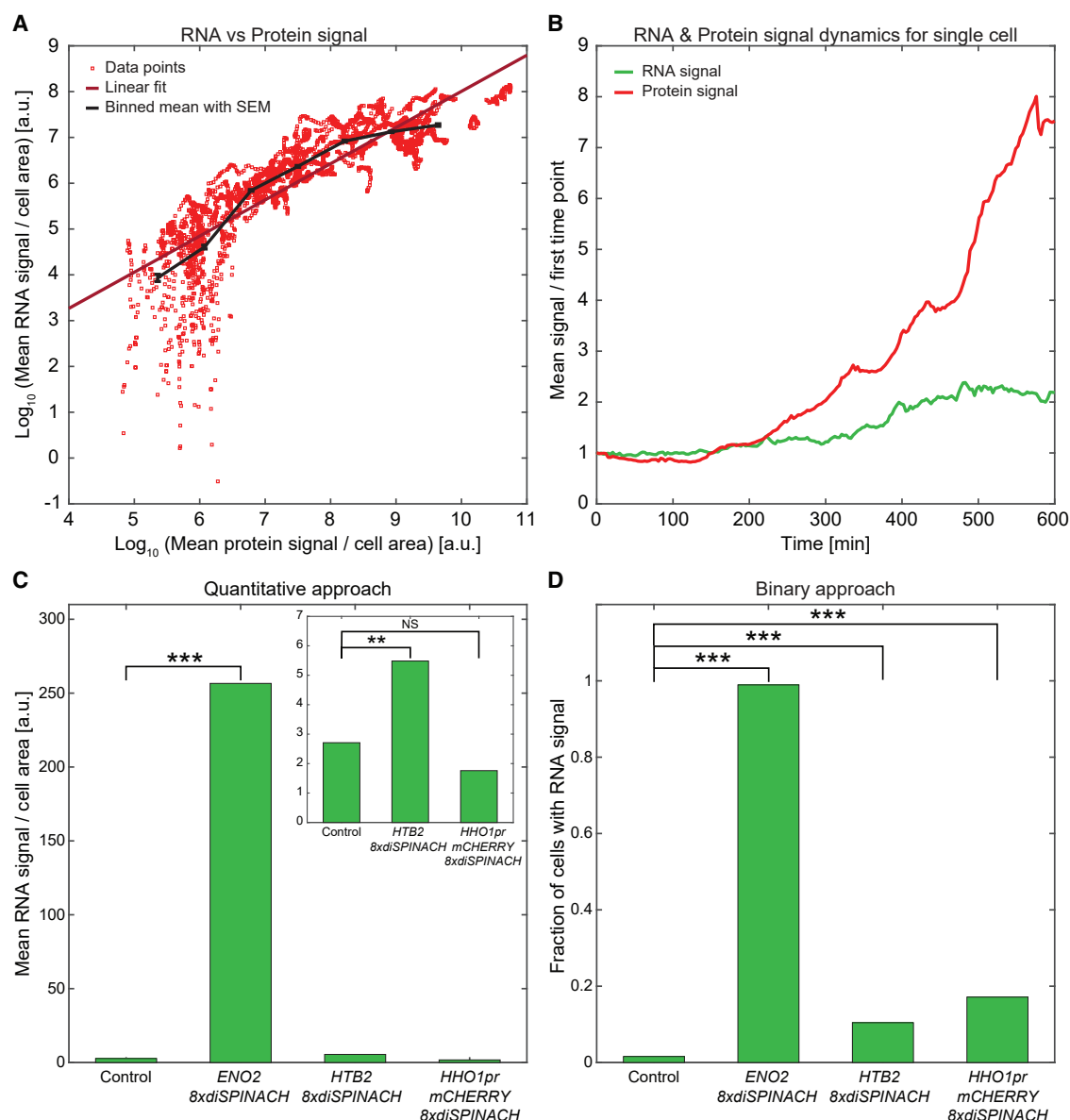
Figure 2. Correlation between RNA (diSpinach) and protein signals in single cells and comparison of two RNA quantification strategies

(A) Mean RNA (diSpinach) signal obtained by applying the quantitative approach, normalized by cell area, as a function of protein signal normalized by cell area in cells transformed with the 2μOri plasmid carrying *ACT1pr-mCherry-8×diSPINACH* ($R = 0.84$, $p < 10^{-30}$). Data from time-lapse experiments were pooled (N = 2,988 cells), and linear regression was fitted to the double-logarithmic data (solid line). Black line, binned means with standard error.

(B) RNA (diSpinach) and protein signals for a representative single cell over 10 h, normalized to the corresponding first time points. Pearson correlation between RNA (diSpinach) and protein signals is $R = 0.92$ ($p < 10^{-30}$).

(C and D) Data from time-lapse experiments pooled for analysis of autofluorescence control (N = 4,627 cells) and strains expressing *ENO2-8×diSPINACH* (N = 6,094 cells), *HTB2-8×diSPINACH* (N = 6,404 cells), and *HHO1pr-mCHERRY-8×diSPINACH* (N = 5,331 cells).

(C) Mean RNA (diSpinach) signals normalized by cell area obtained from the quantitative approach. ***$p < 10^{-30}$ (according to Wilcoxon test and one-way ANOVA with Bonferroni correction), **$p < 10^{-25}$ (Wilcoxon test) or $p < 0.006$ (one-way ANOVA with Bonferroni correction). NS, not significant. Standard errors are smaller than 0.02 [a.u.] and, thus, not visible.

(D) Fraction of cells with detectable RNA (diSpinach) signal, calculated using the binary approach. ***$p < 10^{-30}$ (according to Wilcoxon test and one-way ANOVA with Bonferroni correction).

Mothers and buds were counted as one cell before cytokinesis. Cells were imaged for 10 h in SCD with 50 μM DHFBI-1T.

See also Figures S2, S3, and S4.
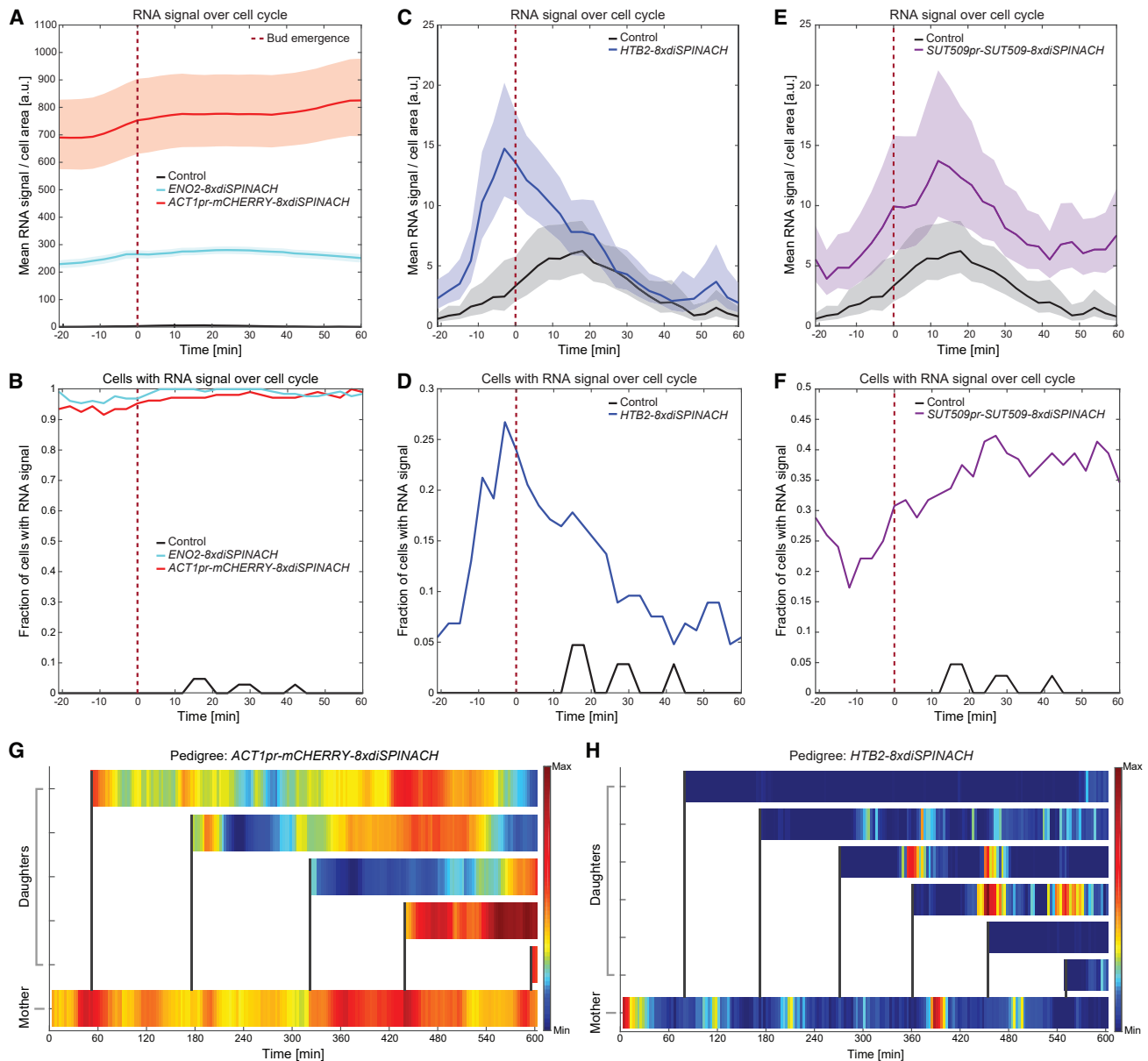
Figure 3. Cell cycle dynamics of RNA (diSpinach) signals

(A–F) Dynamics of RNA (diSpinach) signal over time, obtained by applying the quantitative approach (A, C, and E) or the binary approach (B, D, and F) for indicated RNAs. Shown is visualization of the 8×diSpinach tag. Black line, autofluorescence control. Cell cycles selected for analysis were aligned at bud emergence (red dashed line) and plotted from −21 min (corresponding to the median beginning of G1 phase) to +60 min (corresponding to the median time of cytokinesis). Ribbons in (A), (C), and (E) indicate 95% confidence intervals as determined from 50,000 bootstrap samples.

(A and B) *ACT1pr-mCHERRY-8×diSPINACH* expressed from a 2μOri plasmid (N = 107 cell cycles) and endogenously tagged *ENO2* (N = 130) signals are largely cell cycle independent. Control cells (N = 106 cell cycles) are shown for comparison.

(C and D) Endogenously tagged *HTB2* shows a maximum RNA (diSpinach) signal at bud emergence (N = 146 cell cycles). Control cells (N = 106 cell cycles) are shown for comparison.

(E and F) *SUT509pr-SUT509-8×diSPINACH* expressed from a 2μOri plasmid exhibits cell cycle-dependent RNA (diSpinach) signal with a maximum around G2 (N = 104 cell cycles). Control cells (N = 106 cell cycles) are shown for comparison.

(G and H) Pedigree plots for single mother cells and their progeny over 10 h overlayed with heatmaps of RNA (diSpinach) signal levels. Vertical black lines, cytokinesis times.

(G) Mean RNA (diSpinach) signal intensities obtained for *ACT1pr-mCHERRY-8×diSPINACH* expressed from a 2μOri plasmid do not show obvious temporal patterns.

(H) Mean RNA (diSpinach) signals obtained for *HTB2* show cell cycle-dependent patterns.

Cells were imaged for 10 h in SCD with 50 μM DHFBI-1T. Mothers and their buds were counted as one cell before cytokinesis. See also Figures S2, S3, and S4.

the weaker *HHO1* promoter (Figure S4C). These results are consistent with the previously reported cell cycle regulation of histone genes (Spellman et al., 1998; Eriksson et al., 2012).

An advantage of RNA aptamers is that they do not require a protein to be expressed and, thus, in principle, are applicable to quantify non-coding RNAs (ncRNA) in live cells. To test this, we chose *SUT509* as a model, which has low (Xu et al., 2009) to medium expression (Nadal-Ribelles et al., 2019) and still unknown cell cycle dynamics. We tagged *SUT509* on an expression plasmid containing its own promoter with *8×diSPINACH* and followed ncRNA expression over 10 h. We were able to visually detect diSpinach signal in this strain (Figure S3), and quantification revealed changes in the intensities and the fraction of cells with the signal throughout the cell cycle with a maximum around G2 phase (Figures 3E and 3F). This cell cycle dependence was recapitulated using a smFISH protocol (Figures S4D and S4E). This suggests that our 8×diSpinach-based approach can be used to study protein-coding and ncRNAs and to examine their temporal expression dynamics.

8×diSpinach tagging enables single-cell pedigree analysis of RNA levels

We then wanted to determine whether we can follow RNAs over several cell divisions and perform pedigree analysis. For this, we focused on data obtained for cells expressing *ACT1pr-mCHERRY-8×diSPINACH* from a 2μOri plasmid and their progeny over 10 h. We observed temporal fluctuations in the diSpinach signal for mother and daughter cells (Figure 3G), which could potentially be explained by copy number variability of 2μOri plasmids (Zakian et al., 1979). Leveraging the power of single-cell tracking, we were able to observe a strong correlation of the diSpinach signal in related mother and daughter cells directly after cytokinesis (Pearson $R = 0.87$, $p < 3.2 \times 10^{-5}$). The correlation values decreased to $R = 0.64$ ($p < 0.008$) after 78 min and then became insignificant ($R = 0.48$, $p > 0.068$) (Figures S4F and S4G). For endogenous HTB2 RNA tagged with 8×diSpinach, we found that the diSpinach signal in the mothers and the majority of daughters oscillated in a cell cycle-dependent manner (Figure 3H), consistent with our results above (Figure 3C). Thus, we can robustly follow the diSpinach signal over many cell divisions and determine the inheritance of RNA dynamics within pedigrees.

### Dynamics of RNA transport from mother to daughter cells

Having established an approach to track RNA dynamics through many cell divisions, we investigated RNA transport from mother cells into their buds. We chose *ENO2* as an example of a constitutively expressed gene based on its relatively high expression level, it being non-essential for yeast function, and because Eno2 protein can be tagged without obvious phenotypic effects (Huh et al., 2003; Fuller et al., 2020). We observed robust diSpinach signals for the endogenously tagged ENO2 RNA. We were able to visually observe the movement of diSpinach signal (*ENO2*) from mothers into buds (Videos S1, S2, and S3). For quantification, we analyzed mothers and buds separately, applied the quantitative

approach, and focused our analysis on the time points between bud emergence and the median time of cytokinesis (60 min after bud emergence) (Figure 4A). We found that the mean diSpinach signal in the bud begins to exceed that in the mother 15 min before cytokinesis and continues to increase (Figure 4B), suggesting asymmetric inheritance of ENO2 diSpinach RNA. Calculating the ratio of bud to mother signal (Figure 4C) revealed that, at the time of cytokinesis, the mean RNA signal in the bud is about 1.6-fold higher than in the mother. We also confirmed by fluorescence *in situ* hybridization (FISH) that, although there is an effect of our tagging approach on RNA levels, it does not affect the ratio of bud to mother signal (STAR Methods; Figures S5A–S5C). To be able to visualize ENO2 (and its paralog ENO1) RNAs using a smFISH protocol, we decreased its expression level by changing the carbon source from glucose to glycerol and ethanol. These experiments again showed asymmetric segregation between the mother and bud (Figures S5F–S5H). Northern blot analysis with *ENO2* as a probe confirmed the presence of a major RNA species corresponding to the expected *ENO2* or *ENO2-8×diSPINACH* full-length RNAs (Figure S5D). Using a probe against *diSPINACH* suggests the additional presence of potential RNA cleavage or decay products (Figure S5E) that do not contain the ENO2 coding part.

To investigate potential effects of uneven fluorophore availability between mothers and buds on the asymmetrical inheritance of ENO2 diSpinach RNA, we performed a DFHBI-1T washout experiment and analyzed diSpinach signal dynamics (Figures S6A–S6C). Our results show that, after the start of fluorophore washout, the diSpinach signal drops rapidly and within ~20 min is reduced to 22%–25%. This decrease is comparable between mothers and buds, suggesting that the asymmetry in the diSpinach RNA signal is not simply due to the local fluorophore availability. Next we performed a glucose withdrawal experiment and observed that, upon glucose removal, the RNA signal starts to form bigger foci (Figure S6D), an observation that is in line with previous findings for multiple RNAs encoding glycolytic proteins (Morales-Polanco et al., 2021). These experiments strongly support the applicability of the 8×diSpinach tag to study RNA and its distribution during cell divisions.

We then wanted to determine whether RNA transport mechanisms are responsible for this asymmetric mRNA inheritance. For this, we tracked the diSpinach (*ENO2*) signal upon genetic manipulation of the RNA transport machinery by individually deleting *SHE2*, *SHE3*, and *MYO4*, all implicated in general RNA transport and linked previously to asymmetric mRNA distribution (Müller et al., 2007; Figures 4B and 4C). We observed that, in these mutants, the diSpinach signal increases more slowly in the buds compared with wild-type cells. For all three deletion strains, the diSpinach signal in the bud never exceeds the signal in the mother (Figures 4B and 4C). Through FISH experiments, we confirmed that deletion of *SHE2* results in a lower daughter-to-mother ratio of the ENO RNA signal compared with wild-type cells (STAR Methods; Figures S5A and S5C). Because Myo4 is a type V myosin motor that conducts an active transport function, She2 co-transcriptionally binds to mRNAs, and She3 acts as an adaptor protein that specifically binds Myo4 and She2 (Müller et al., 2007), our results suggest that ENO2 diSpinach RNAs are actively transported in a myosin-dependent manner. Upon
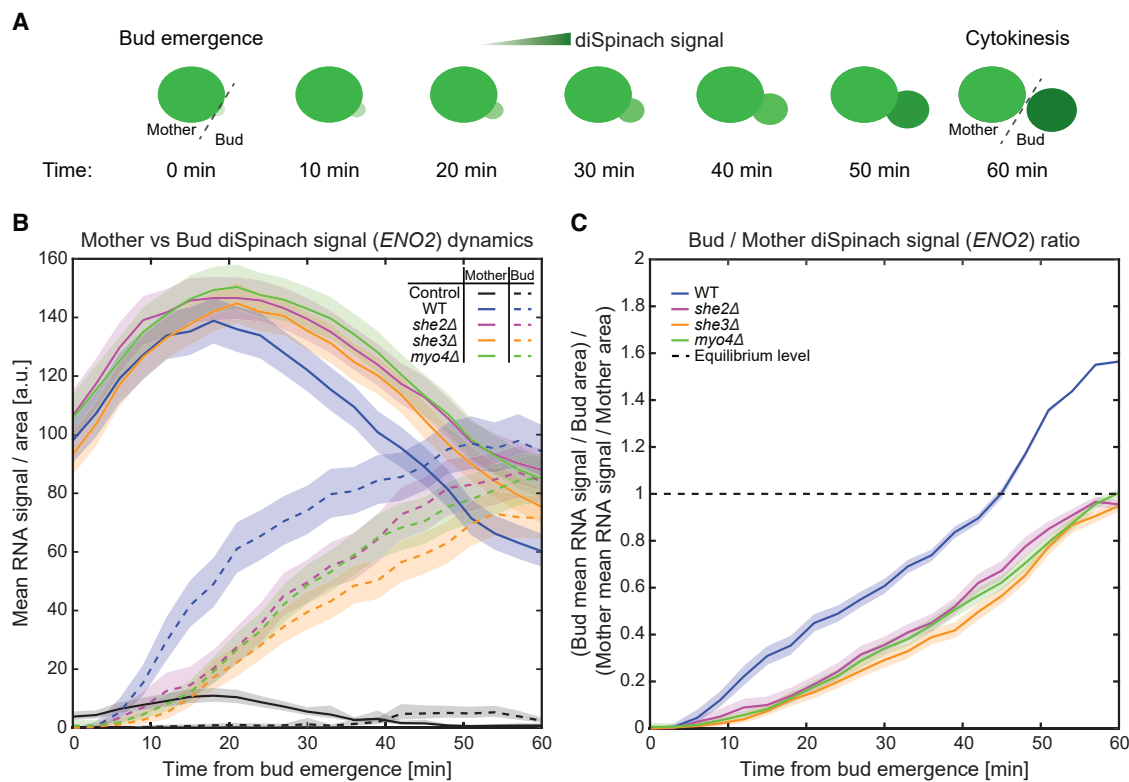
Figure 4. Dynamics of diSpinach signal (*ENO2*) transport into buds

(A) Schematic of the ENO2 diSpinach RNA analysis.

(B) Dynamics of mean diSpinach signal (*ENO2*) in mothers and buds (solid and dashed lines) normalized by corresponding cell area, aligned at bud emergence, shown until the median cytokinesis time point (+60 min). Wild-type (*ENO2-8×diSPINACH* cells, N = 224 cell cycles, blue) and 3 RNA transport machinery mutants (*she2Δ* [N = 224 cell cycles, magenta], *she3Δ* [N = 251 cell cycles, orange], *myo4Δ* [N = 302 cell cycles, green]). Autofluorescence control (N = 240 cell cycles) is shown in black. Very low signal in early buds is most likely due to thresholding in the quantitative analysis.

(C) Ratios of the normalized mean signal intensities for buds and mothers plotted in (B). Dashed line, ratio at which mean RNA (diSpinach) signals in buds and mothers are equal.

Cells were imaged for 10 h in SCD with 50 μM DHFBI-1T. Mothers and buds were counted as separate cells from bud emergence. Ribbons, 95% confidence intervals determined from 50,000 bootstrap samples. See also Figures S3, S5, and S6.

deletion of *MYO4*, *SHE2*, or *SHE3*, active transport along actin cables is most likely disrupted, and, consistent with transport based on diffusion, the diSpinach signals in the bud and mother reach similar intensities at cytokinesis.

To address how our observations for ENO2 diSpinach RNA are reflected on the protein level, we tagged Eno2 with the fluorescent protein mCherry. As shown in Figures S6E and S6F, we did not detect obvious asymmetric inheritance for Eno2 protein, suggesting that the localization of RNA and protein are not coupled. We also obtained a similar result for Eno2 tagged with sfGFP (Figures S6G and S6H). Eno2 protein distribution is not visibly affected in *she2Δ* cells.

To address whether the asymmetric inheritance of RNA we observed is limited to glycolytic genes, we tagged another glycolytic gene, *PDC1* (pyruvate decarboxylase isozyme 1), as well as a non-glycolytic gene, *TEF1* (translation elongation factor EF-1 alpha), with *8×diSPINACH* and imaged diSpinach intensities. We found that the PDC1 diSpinach signal also has a tendency toward asymmetric inheritance, but less pronounced (~1.2-fold) than that observed for ENO2 diSpinach, whereas TEF1 diSpi-

nach signal exhibits asymmetry that is stronger (~2.7-fold) than that of ENO2 diSpinach (Figure 5). Upon deletion of *MYO4* or *SHE2*, TEF1 diSpinach signal increases slower in the buds compared with wild-type cells (Figures 5C and 5D). This highlights again that active transport machinery is involved in asymmetric RNA segregation. We observed no preferential diSpinach signal distribution toward daughters in cells with *ACT1pr-mCHERRY-8×diSPINACH* expressed from a 2μOri plasmid (Figures S1E and S1F).

Our results suggest first that ENO2 diSpinach RNA is actively transported from the mother into its bud, resulting in asymmetric distribution with an increased RNA level in the bud just prior to cytokinesis, and second that this asymmetric inheritance is not limited to glycolytic genes.

Change in asymmetric distribution of RNA during replicative aging

It has been shown previously that the symmetry of protein distribution between mothers and daughters can change with aging (Erjavec et al., 2007; Morlot et al., 2019). In particular, the
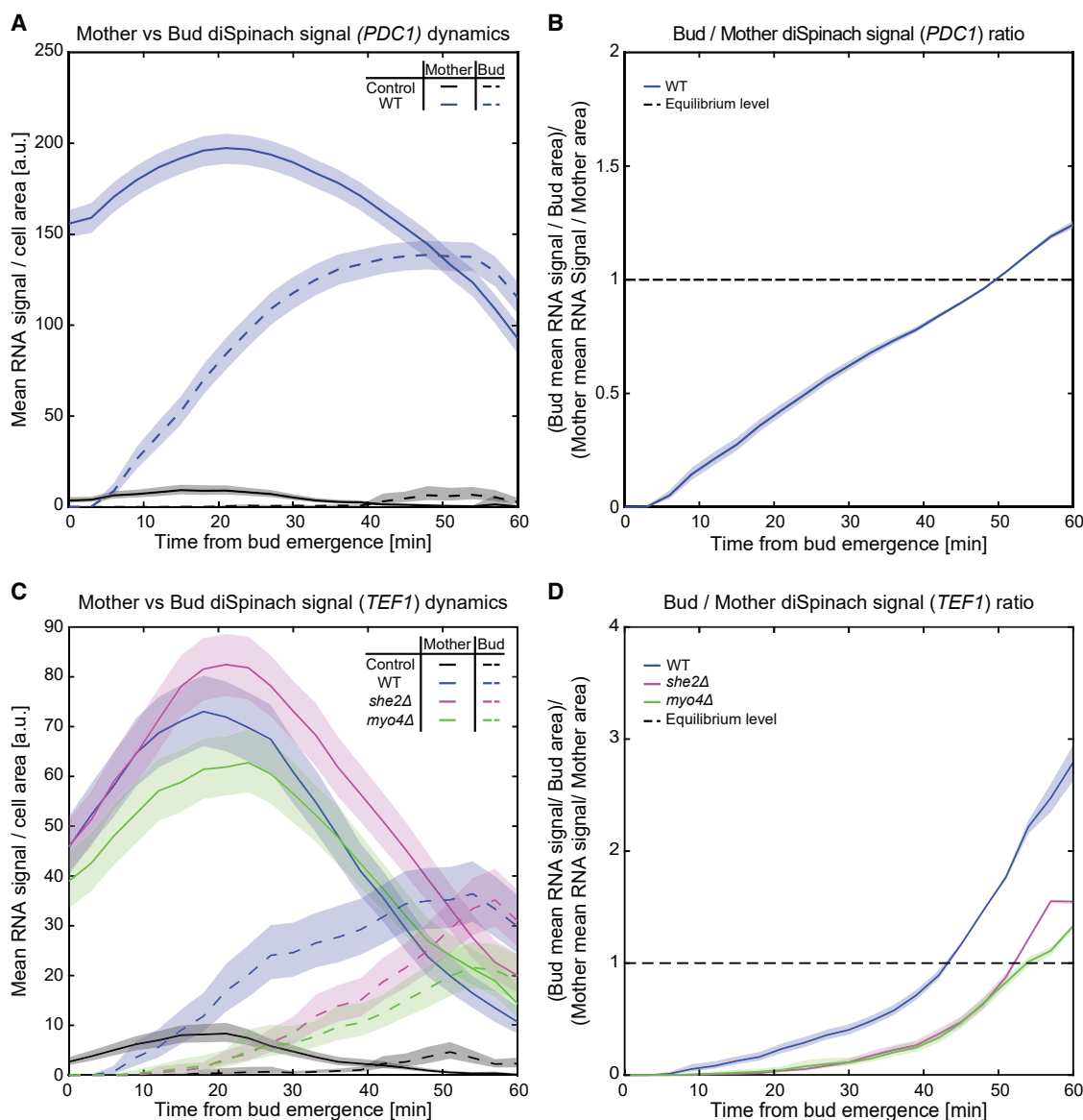
Figure 5. Dynamics of diSpinach signal (*PDC1* and *TEF1*) transport into buds

(A and C) Dynamics of mean diSpinach signal for *PDC1* and *TEF1* in mothers and buds (solid and dashed lines) normalized by corresponding cell area, aligned at bud emergence, shown until the median cytokinesis time point (+ 60 min).

(A) *PDC1* plot: autofluorescence control (N = 203 cell cycles, black) and wild type (*PDC1-8×diSPINACH*, N = 307 cell cycles, blue).

(C) *TEF1* plot: autofluorescence control (N = 302 cell cycles, black), wild type (*TEF1-8×diSPINACH*, N = 200 cell cycles, blue), and transport mutants (*she2Δ* [N = 203 cell cycles, magenta] and *myo4Δ* [N = 204 cell cycles, green]).

(B and D) Ratios of the normalized mean signal intensities for buds and mothers. Dashed line, ratio at which mean RNA (diSpinach) signals in buds and mothers are equal.

Cells were imaged for 10 h in SCD with 50 μM DHFBI-1T. Mothers and buds were counted as separate cells from bud emergence. Ribbons, 95% confidence intervals determined from 50,000 bootstrap samples. See also Figures S1 and S3.

oxidized form of the Eno2 protein is preferentially retained in mothers and has been linked to replicative aging (Erjavec et al., 2007). For this reason, we decided to test whether the asymmetric distribution of ENO2 diSpinach signal between mothers and daughters at cytokinesis also changes during replicative aging. Thus, we carried out time-lapse experiments with a duration of up to 72 h (Video S4), using a microfluidics device de-

signed to study aging in yeast (Morlot et al., 2019; Goulev et al., 2017). We analyzed the RNA signal in aging mothers and their corresponding daughters at cytokinesis time points (Figure 6A) by applying the quantitative approach and found that the mean diSpinach signal in mothers stays largely constant over at least 16 divisions. In the corresponding daughters, the signal is largely constant for the first 8 of these divisions but then decreases and
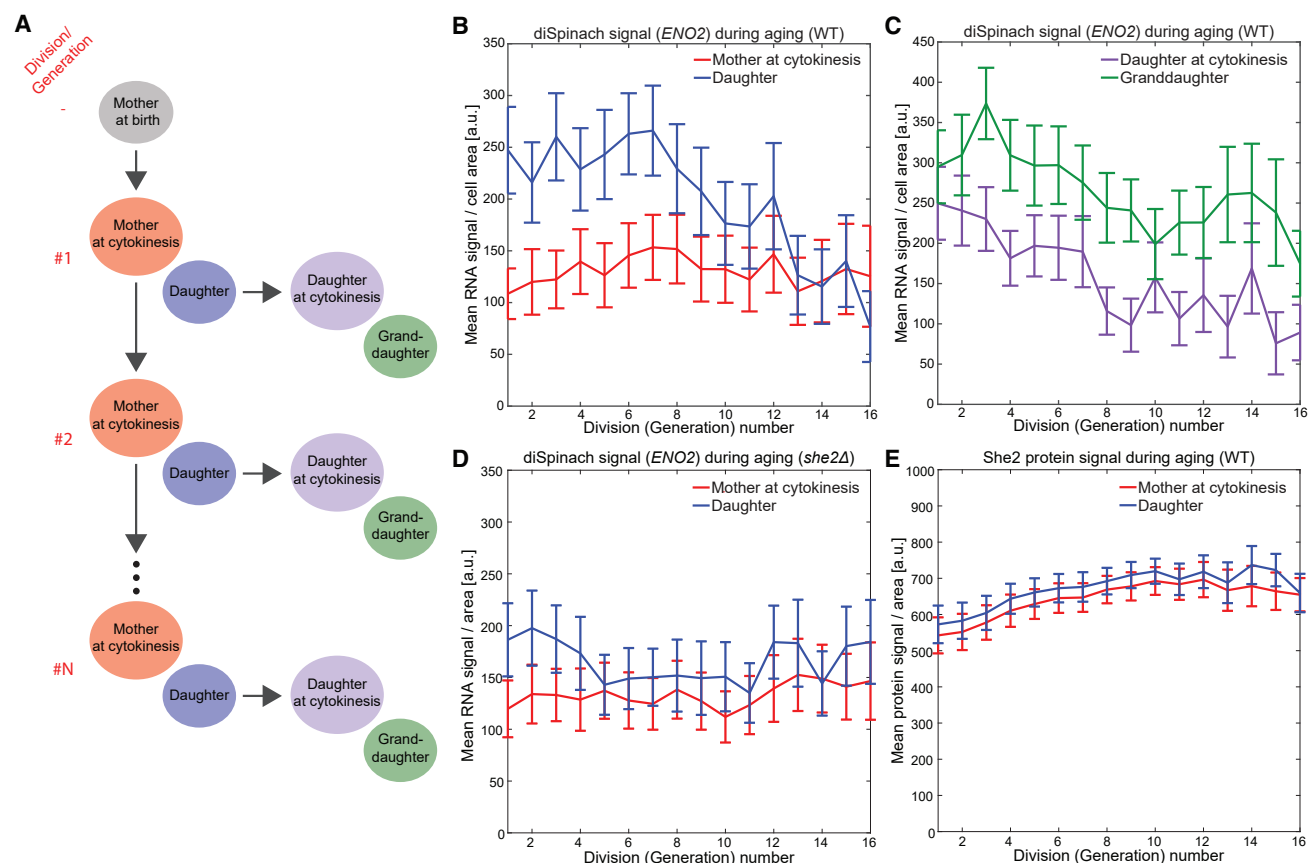
Figure 6. Loss of asymmetric RNA inheritance during replicative aging

(A) Schematic of aging experiments. Shown are division (generation) numbers, mother cells at cytokinesis (red), their daughters (blue), the daughters at cytokinesis (purple), and their daughters (granddaughters, green).

(B) Mean diSpinach signal (*ENO2*) in mothers at cytokinesis (N = 40 cell tracks, red) and their daughters (N = 40 cell tracks, blue), normalized by corresponding cell area, plotted against mother cell division (daughter generation) numbers for the wild type.

(C) Mean diSpinach signal (*ENO2*) in daughters at cytokinesis (N = 551 cells of different generations separated from their mothers at corresponding divisions, purple) and granddaughters (N = 547 newly born cells, green), normalized by corresponding cell area, plotted against division (generation) number for the wild type.

(D) Mean diSpinach signal (*ENO2*) in mothers at cytokinesis (N = 40 cell tracks, red) and their daughters (N = 40 cell tracks, blue), normalized by corresponding cell area, plotted against mother cell division (daughter generation) numbers for the *she2Δ* strain.

(E) Mean She2 protein signal in mothers at cytokinesis (N = 41 cell tracks, red) and their daughters (N = 41 cell tracks, blue), normalized by corresponding cell area, plotted against mother cell division (daughter generation) numbers for the She2-mCherry strain.

Cells were grown in SCD with 50 μM DHFBI-1T and imaged for up to 72 h. Whiskers (B–E) show standard errors. See also Figure S7.

reaches the same level as in the mothers around generation 16 (Figures 6B and S7A). This suggests that the preferential inheritance of ENO2 diSpinach transcripts by daughter cells at cytokinesis declines during replicative aging of the mother cell.

Next we wanted to determine whether this loss of asymmetry during replicative aging is immediately restored in the first division of daughter cells (Figure 6A). We found that, although the mean diSpinach signal in the daughter and granddaughter cells decreases and then stays largely constant with the mother cell divisions, the asymmetry of ENO2 diSpinach RNA signal is maintained in the progeny of old mothers (Figure 6C). This observation is in line with the concept of daughter cell rejuvenation (Unal et al., 2011).

Our data suggest that ENO2 diSpinach RNA levels at cytokinesis in mother cells stay largely constant over multiple divisions, whereas its preferential distribution to daughter cells starts to decrease as early as division 8 of the mother cell, resulting in loss of asymmetric RNA inheritance.

Role of active transport in asymmetric RNA distribution during replicative aging

To investigate how active transport is involved in the asymmetric inheritance of ENO2 diSpinach RNA signal and its loss with replicative aging, we performed additional aging experiments using *she2Δ* cells. We found that, in these cells, the degree of RNA asymmetric segregation between mother and daughter cells is already much less pronounced starting from younger generations and stays largely constant during aging (Figure 6D). This result supports our previous finding that active RNA transport is required for asymmetric RNA inheritance and suggests that

asymmetry may be lost during replicative aging because of a switch from active to predominantly diffusion-based transport (Figure 4). Next we endogenously tagged She2 with mCherry and examined whether the levels of She2 proteins decrease with age. We found that She2 protein levels remained the same between mothers and daughters and were relatively constant during aging (Figure 6E). These results suggest that, although RNA transport via the She2-related machinery is needed for the asymmetric transport of ENO2 diSpinach RNA, changes in She2 protein levels do not account for the age-dependent loss of asymmetric RNA inheritance.

Effect of cell morphology and cell cycle duration on asymmetric RNA distribution during replicative aging

Replicative aging goes along with changes in cell morphology, such as size or geometry, and cell cycle duration (Mortimer and Johnston, 1959; Jo et al., 2015; Li et al., 2020). We thus wondered whether these changes could explain the shift in the asymmetric segregation of ENO2 diSpinach signal. We observed in later cell divisions/generations an increase in cell size (Figures S7B–S7D) as well as a change in the geometry of mothers (more round) and daughters (more elongated) with pronounced alterations in daughter cell shape (Figures S7E–S7J). The increase in the mother cell area is inversely correlated with changes in the daughter/mother diSpinach signal ratio (Figure S7D; Pearson correlation $R = -0.94$, p = $\sim10^{-7}$), whereas the mean RNA signal in mother cells stays roughly at a constant level independent of the cell area (Figure S7C). Similarly, we observed that the alterations in daughter cell shape are correlated with lower diSpinach signal in the daughters (Figures S7I and S7J) because we found a clear inverse correlation between daughter/mother signal ratio and daughter geometry (Figure S7F; Pearson correlation $R = -0.93$, p < 10^{-6}). There is an increase in cell cycle duration in older mother cells (approximately divisions 10–16) but not in daughter cells (Figure S7K). Again, we observed that loss of asymmetric RNA segregation is inversely correlated with changes in the cell cycle duration of mother cells (Figure S7L; Pearson correlation $R = -0.84$, p < 10^{-4}) but not correlated with changes in the duration of the cell cycle of newly born daughter cells (Figure S7L; Pearson correlation $R = 0.17$, p = 0.53).

Having detected a correlation between cell geometry, cell cycle duration, cell size, and replicative age with loss of asymmetric RNA inheritance, we then investigated which of these parameters is the most predictive for this phenomenon using multi-variable regression (STAR Methods). We found that only replicative age (p = 0.029) and mother cell area (p = 0.046), but not cell geometry (p = 0.795) or duration of mother S-G2-M phase (p = 0.132), are significantly predictive. This suggests that aging and/or cell size might be causal for the reduction of ENO2 diSpinach signal in the daughter cells and the loss of asymmetric inheritance. In fact, recent studies have causally linked large cell size to the impaired function of old cells (Neurohr et al., 2019; Lengefeld et al., 2021).

Effect of cell size on asymmetric RNA distribution

To experimentally test whether the increased cell size is the key determinant explaining the loss of asymmetric ENO2 diSpinach

signal at cytokinesis observed during replicative aging, we employed a previously established approach to genetically manipulate cell size (Kukhtevich et al., 2020; Claude et al., 2021; Figure 7A). Inducible expression of Whi5 allows strong alterations in steady-state cell size without major effects on population doubling time. In the absence of the inducer β-estradiol, Whi5-inducible cells are slightly smaller than wild-type cells, whereas addition of β-estradiol results in steady-state populations with an ∼2-fold increase in average cell size (STAR Methods). Therefore, we omitted β-estradiol from the medium or supplemented it with one dose of 400 nM β-estradiol overnight to generate young cells with a wide range of sizes and then performed time-lapse experiments. We next calculated the mean ENO2 diSpinach signal for newly born cells at cytokinesis of their first cell cycle and analyzed the RNA signal as a function of cell area (Figures 7B and 7C). Similar to aging mothers, the mean diSpinach signal for young mothers stays largely constant independent of cell area (Figure 7B). In contrast to the decrease of diSpinach signal in daughters of aging mothers, in daughters of young mothers, the diSpinach signal does not decrease with cell area (Figure 7C). These data suggest that, in the case of young cells, ENO2 diSpinach RNA is inherited asymmetrically by daughters independent of cell size.

We observed a loss of asymmetry in RNA distribution during replicative aging, which is not a direct consequence of increased cell size but rather due to additional aging-related processes (Figure 7E) that can be restored during rejuvenation of daughter cells.

Effect of Sir2 protein on age-dependent asymmetric RNA distribution

Because our findings suggest that loss of asymmetric inheritance of ENO2 diSpinach RNA during aging is mainly linked to division/generation number, we next examined the age-dependent segregation dynamics of the diSpinach signal in short-lived cells. To accomplish this, we deleted the lifespan determinant Sir2 (Wierman and Smith, 2014). We found that in *sir2Δ* cells, mothers and daughters have almost identical diSpinach signals for ENO2 RNA from the very first divisions onward, indicating a lack of asymmetric inheritance in this mutant (Figure 7D). Thus, *sir2Δ* cells fully resemble aged wild-type mother cells with respect to diSpinach signal distribution. This finding is in line with previous reports showing that *sir2Δ* cells exhibit a loss of asymmetric segregation of oxidatively damaged proteins, mitochondria, and repair machinery between mother and daughter cells (Wierman and Smith, 2014).

Our findings suggest that Sir2, in addition to controlling the asymmetric distribution of oxidized Eno2 protein (Erjavec et al., 2007), may also be required for the asymmetric inheritance of ENO2 diSpinach RNA during aging (Figure 7E).

DISCUSSION

Here we followed, for the first time, the inheritance of RNA over multiple generations in single cells, comparing aged and young mother cells and their daughters and granddaughters. For this, we tagged endogenous RNAs with eight repeats of the RNA aptamer diSpinach and performed time-lapse imaging in
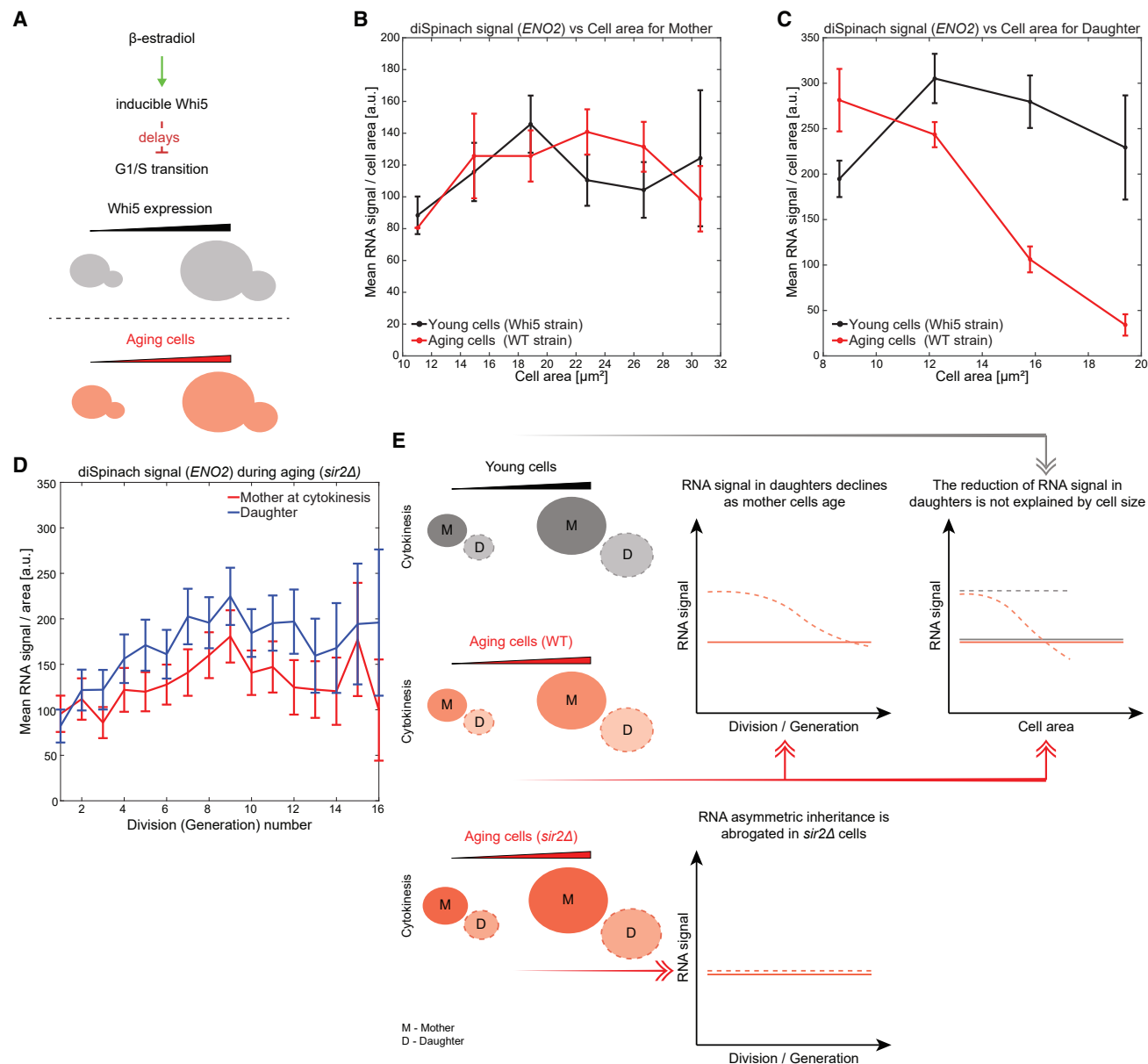
Figure 7. Effect of cell size and reduction of replicative potential on the asymmetric diSpinach signal (ENO2) inheritance during replicative aging

(A) Schematic of genetic manipulation of cell size in young cells by controlling Whi5 expression. For details, see text.

(B) Mean diSpianch signal (ENO2) per cell area at cytokinesis in young mothers for the Whi5-inducible strain (N = 289 cells at the first division, black) and aging wild-type mothers (N = 646 cells with different division numbers, red) as a function of cell area.

(C) Mean diSpinach signal (ENO2) per cell area at cytokinesis in young daughters for the Whi5-inducible strain (N = 289 cells at the first division, black) and wild-type daughters during aging experiments (N = 646 cells of different generations, red) as a function of cell area.

(D) Mean diSpinach signal (ENO2) in mothers at cytokinesis (N = 50 cell tracks, red) and their daughters (N = 50 cell tracks, blue), normalized by corresponding cell area, plotted against mother cell division (daughter generation) numbers for the sir2Δ strain.

Cells were grown in SCD with 50 μM DHFBI-1T and imaged for up to 72 h for aging experiments with the wild-type and sir2Δ strains and 10 h with the Whi5-inducible strain. Whiskers (B–D) show standard errors.

(E) Schematic summary of asymmetric ENO2 diSpinach signal inheritance during replicative aging. For details, see text. Cell size alone does not account for the age-dependent decline of RNA inheritance to daughters. In the case of sir2Δ cells, the asymmetric RNA inheritance is abrogated.

See also Figure S7.

a custom-made, multi-chamber microfluidics device (Figure 1A). Critical for the questions addressed here, and in contrast to commonly used endpoint analyses, the live-cell character of our RNA visualization approach makes it possible to incorporate the history of the individual cells into the analysis.

While establishing our approach, we observed that the distribution of the RNA signal within cells can vary strongly (Figure S3). In addition to different numbers of foci/spots per cell, we observed cells with different spot morphologies, ranging from a clear maximum of intensity in distinct foci to larger rather diffuse signals and cells with simply overall increased fluorescence intensity within the cell contours, potentially because of a large number of broadly distributed RNAs. Thus, we had to develop pipelines to quantify the intensity of the RNA signal for high, medium, and low RNA expression levels, which we achieved with the "quantitative" and "binary" approaches, respectively.

Using an MS2-based approach, Lui et al. (2014) also reported a punctuated localization pattern for ENO2 RNA. Morales-Polanco et al. (2021) demonstrated a granular localization pattern of multiple glycolytic mRNAs (including *ENO2* and *PDC1*) and suggested that being "housed in large cytoplasmic bodies" is a feature of mRNAs of many glycolytic genes. It is still unclear how many RNA molecules are harbored by the foci we observed with the diSpinach-based imaging approach and whether these are indeed full-length RNAs.

Our study provides, for the first time, evidence that ENO2 diSpinach RNAs are actively transported from the mother into the bud in a Myo4-, She2-, and She3-dependent manner, resulting in an asymmetric distribution at cytokinesis with a significantly elevated RNA signal in the bud compared with the mother cell (Figure 4). For PDC1 and TEF1 the diSpinach RNA signal seem to be asymmetrically distributed at cytokinesis, but the levels of asymmetry are different in comparison with ENO2 diSpinach RNA (Figure 5). These results, together with data on ASH1 RNA (Heym and Niessing, 2012; Haber, 2012), HXT2 RNA (Stahl et al., 2019) and CLB2 RNA asymmetric distribution (Tutucci et al., 2022), suggest that asymmetric inheritance of RNA could be widespread and is not limited to glycolytic genes. The Eno2 protein behavior is not recapitulating the asymmetry we observed for the RNA, something that has also been described recently for Clb2 protein (Tutucci et al., 2022).

We observed that asymmetric RNA inheritance changes in *ENO2-8×diSPINACH* cells with replicative age. In aging mothers, diSpinach signal levels at cytokinesis are largely independent of division number, whereas they decrease in daughter cells with increasing generation number, resulting in loss of asymmetric inheritance (Figure 7E). Our cell size manipulation experiments suggest that in daughters of young mothers, ENO2 diSpinach signal is largely independent of cell size, and asymmetric distribution is maintained even in bigger cells (Figure 7C). Thus, increased cell size alone does not explain the loss of asymmetric RNA inheritance into daughters during replicative aging. We did not find any signs that the transport machinery itself is affected during replicative aging; She2 protein levels remained largely constant in mothers and daughters (Figure 6E) and are most likely not determining the age-dependent loss of asymmetric RNA inheritance. However, we cannot exclude

changes of other components of the transport machinery (such as She3 or Myo4), F-actin, or ATP levels. Our data suggest that Sir2 is required for asymmetric inheritance (Figures 7D and 7E) of ENO2 diSpinach RNA, and this is in line with the previously described function of Sir2 in establishing cellular age asymmetry that might lead to daughter cell rejuvenation (Aguilaniu et al., 2003; Liu et al., 2010). Consistent with our findings, Sir2 protein abundance progressively decreases in mother cells during replicative aging, with the most significant reduction occurring at division numbers coinciding with the loss of asymmetric RNA inheritance (Dang et al., 2009).

Our northern blot analysis using a probe against *diSPINACH* indicates the additional presence of potential RNA decay/cleavage products (Figures S1D and S5E). It is conceivable that these could affect imaging results. However, northern blots only provide an average snapshot of RNA size and no information about the localization of these fragments or accumulation in a subpopulation of cells. Crucially, though, we did not observe asymmetric inheritance of diSpinach signal for *mCHERRY* tagged with *8×diSPINACH* (Figures S1E and S1F), suggesting that asymmetric inheritance is not simply due to the presence of decay/cleavage products. Similar RNA decay products have been observed in northern blot analyses of the original versions of MS2 tags, and they have been discussed in multiple publications (Garcia and Parker, 2015, 2016; Haimovich et al., 2016; Heinrich et al., 2017). The presence of RNA decay products has been mitigated by a re-engineered version of the MS2 tag (Tutucci et al., 2018), suggesting that future engineering of diSpinach tags might be beneficial. Thus, we advocate a cautionary approach when using diSpinach; in particular, validation of results should be performed using orthogonal methods such as FISH or smFISH. Our FISH experiments for endogenous untagged ENO RNAs (Figures S5F–S5H) confirmed their increased level in buds compared with mothers. We consider it unlikely that the observed loss of ENO2 asymmetry in transport mutants or during aging occurs simply because of preferential loss of RNA decay/cleavage products, but at this time, we cannot formally exclude this possibility.

RNA imaging as described here opens opportunities to study RNA transport and inheritance in live budding yeast at the single-cell level to reveal regulatory principles, which are potentially conserved across species. The asymmetric inheritance of cellular components such as RNA could lead to different cell states of the two resulting cells. Because these cell states can affect cellular responses to external stimuli, they are critical for the survival and fitness of unicellular organisms such as *S. cerevisiae* as well as development and homeostasis of multicellular organisms. Thus, the approach we describe here could also be used to address key questions about phenotypic heterogeneity in different organisms.

Limitations of the study

Specific RNA motifs such as MS2 (Tyagi, 2007) or PP7 (Lenstra and Larson, 2016) have often been used for live detection of RNAs and have enabled many discoveries in transcriptional dynamics. The MS2/PP7 system as well as RNA aptamer-based imaging approaches rely on genetic insertions and recruitment of coat proteins coupled to fluorescent proteins or binding to

fluorophores. Therefore, potential biological effects as a result of altered stability, turnover of the RNA itself, or expression should be taken into account for each RNA studied. Both of these approaches have different caveats that have to be carefully considered; in particular, potential accumulation of mRNA cleavage or decay products because of RNA tagging. In the case of the diSpinach aptamer system, some of the caveats are mitigated by use of fluorophores, like DHFBI-1T, because these molecules are approximately 100 times smaller than, e.g., coat proteins and generate fluorescence signals only upon RNA binding. However, RNA aptamers have other disadvantages. Specifically, the aptamer system has limitations for counting RNA molecules as well as multicolor imaging and has lower brightness, which is potentially a constraint for imaging and tracking lowly expressed RNAs. High numbers of aptamer repeats may increase the sensitivity of detection but could have undesirable effects on the cells or the RNA itself. Thus, the choice of approach should take into consideration these caveats and be based on the RNA under investigation.

STAR★METHODS

Detailed methods are provided in the online version of this paper and include the following:

- KEY RESOURCES TABLE
- RESOURCE AVAILABILITY
  - Lead contact
  - Materials availability
  - Data and code availability
- EXPERIMENTAL MODEL AND SUBJECT DETAILS
- METHOD DETAILS
  - Strain construction
  - Aptamer-based tagging strategy
  - Growth conditions
  - Microfluidic devices
  - Well-device
  - Live-cell microscopy
  - FISH experiments for ENO2 RNA in SCD
  - FISH experiments for ENO2 RNA in SCGE and SUT509 in SCD
  - Impact of aptamer-based tagging on RNA
  - Northern blot
- QUANTIFICATION AND STATISTICAL ANALYSIS
  - Cell segmentation
  - Image processing
  - Cell autofluorescence control
  - Quantification of the RNA and protein signals
  - Signal normalization
  - Correlation analysis
  - Multi-variable linear regression
  - Testing different numbers of diSpinach repeats
  - 8xdiSpinach effect on expression from 2 μOri plasmids
  - Endogenous tagging with diSpinach repeats
  - Cell cycle analysis
  - Single-cell pedigree analysis
  - Analysis of RNA transport from a mother into its bud and corresponding protein levels

  - Analysis of fluorophore availability in cells during time-lapse experiments
  - Analysis of experiments relating to replicative aging and cell size
  - FISH data analysis for ENO2 RNA in SCGE/SUT509 in SCD

AUTHOR CONTRIBUTIONS

I.V.K. and R.S. initiated the project. C.D. provided the diSpinach sequence. I.V.K. designed the microfluidics device and established the pipeline for RNA imaging and image analysis. I.V.K., P.B., A.K., K.M.S., Y.C., S.H., and R.S. designed all experiments. I.V.K. performed the majority of experiments. I.V.K., M.R.-R., and N.R. performed experiments on RNA transport from mothers into buds. I.V.K. and N.R. performed aging experiments. P.B. and Y.C. performed FISH experiments. S.H. performed northern blots. D.B. and S.D. performed validation experiments. I.V.K., M.R.-R., N.R., Y.C., and P.R.-B. analyzed all experimental data. K.M.S. contributed to data analysis. I.V.K., P.B., C.D., Y.C., A.K., K.M.S., and R.S wrote the paper.

DECLARATION OF INTERESTS

The authors declare no competing interests.

INCLUSION AND DIVERSITY

All authors support inclusive, diverse, and equitable conduct of research.

REFERENCES

Aguilaniu, H., Gustafsson, L., Rigoulet, M., and Nyström, T. (2003). Asymmetric inheritance of oxidatively damaged proteins during cytokinesis. Science 299, 1751–1753. https://doi.org/10.1126/science.1080418.

Autour, A., C Y Jeng, S., D Cawte, A., Abdolahzadeh, A., Galli, A., Panchapakesan, S.S.S., Rueda, D., Ryckelynck, M., and Unrau, P.J. (2018). Fluorogenic RNA Mango aptamers for imaging small non-coding RNAs in mammalian cells. Nat. Commun. 9, 656. https://doi.org/10.1038/s41467-018-02993-8.

Autour, A., Westhof, E., and Ryckelynck, M. (2016). iSpinach: a fluorogenic RNA aptamer optimized for in vitro applications. Nucleic Acids Res. *44*, 2491–2500. https://doi.org/10.1093/nar/gkw083.

Bouhedda, F., Autour, A., and Ryckelynck, M. (2017). Light-up RNA aptamers and their cognate fluorogens: from their development to their applications. Int. J. Mol. Sci. *19*, 44. https://doi.org/10.3390/ijms19010044.

Bratu, D.P., Cha, B.J., Mhlanga, M.M., Kramer, F.R., and Tyagi, S. (2003). Visualizing the distribution and transport of mRNAs in living cells. Proc. Natl. Acad. Sci. USA *100*, 13308–13313. https://doi.org/10.1073/pnas.2233244100.

Brown, T., Howe, F.S., Murray, S.C., Wouters, M., Lorenz, P., Seward, E., Rata, S., Angel, A., and Mellor, J. (2018). Antisense transcription-dependent chromatin signature modulates sense transcript dynamics. Mol. Syst. Biol. *14*, e8007. https://doi.org/10.15252/msb.20178007.

Chen, X., Zhang, D., Su, N., Bao, B., Xie, X., Zuo, F., Yang, L., Wang, H., Jiang, L., Lin, Q., et al. (2019). Visualizing RNA dynamics in live cells with bright and stable fluorescent RNAs. Nat. Biotechnol. *37*, 1287–1293. https://doi.org/10.1038/s41587-019-0249-1.

Chernova, T.A., Wilkinson, K.D., and Chernoff, Y.O. (2014). Physiological and environmental control of yeast prions. FEMS Microbiol. Rev. *38*, 326–344. https://doi.org/10.1111/1574-6976.12053.

Claude, K.-L., Bureik, D., Chatzitheodoridou, D., Adarska, P., Singh, A., and Schmoller, K.M. (2021). Transcription coordinates histone amounts and genome content. Nat. Commun. *12*, 4202. https://doi.org/10.1038/s41467-021-24451-8.

Costanzo, M., Nishikawa, J.L., Tang, X., Millman, J.S., Schub, O., Breitkreuz, K., Dewar, D., Rupes, I., Andrews, B., and Tyers, M. (2004). CDK activity antagonizes Whi5, an inhibitor of G1/S transcription in yeast. Cell *117*, 899–913. https://doi.org/10.1016/j.cell.2004.05.024.

Dang, W., Steffen, K.K., Perry, R., Dorsey, J.A., Johnson, F.B., Shilatifard, A., Kaeberlein, M., Kennedy, B.K., and Berger, S.L. (2009). Histone H4 lysine 16 acetylation regulates cellular lifespan. Nature *459*, 802–807. https://doi.org/10.1038/nature08085.

de Bruin, R.A.M., McDonald, W.H., Kalashnikova, T.I., Yates, J., 3rd, and Wittenberg, C. (2004). Cln3 activates G1-specific transcription via phosphorylation of the SBF bound repressor Whi5. Cell *117*, 887–898. https://doi.org/10.1016/j.cell.2004.05.025.

Denoth-Lippuner, A., Krzyzanowski, M.K., Stober, C., and Barral, Y. (2014). Role of SAGA in the asymmetric segregation of DNA circles during yeast ageing. Elife *3*, e03790. https://doi.org/10.7554/eLife.03790.

Dietler, N., Minder, M., Gligorovski, V., Economou, A.M., Joly, D.A.H.L., Sadeghi, A., Chan, C.H.M., Koziński, M., Weigert, M., Bitbol, A.-F., and Rahi, S.J. (2020). A convolutional neural network segments yeast microscopy images with high accuracy. Nat. Commun. *11*, 5723. https://doi.org/10.1038/s41467-020-19557-4.

Dolgosheina, E.V., Jeng, S.C.Y., Panchapakesan, S.S.S., Cojocaru, R., Chen, P.S.K., Wilson, P.D., Hawkins, N., Wiggins, P.A., and Unrau, P.J. (2014). RNA mango aptamer-fluorophore: a bright, high-affinity complex for RNA labeling and tracking. ACS Chem. Biol. *9*, 2412–2420. https://doi.org/10.1021/cb500499x.

Entelis, N., Brandina, I., Kamenski, P., Krasheninnikov, I.A., Martin, R.P., and Tarassov, I. (2006). A glycolytic enzyme, enolase, is recruited as a cofactor of tRNA targeting toward mitochondria in Saccharomyces cerevisiae. Genes Dev. *20*, 1609–1620. https://doi.org/10.1101/gad.385706.

Eriksson, P.R., Ganguli, D., Nagarajavel, V., and Clark, D.J. (2012). Regulation of histone gene expression in budding yeast. Genetics *191*, 7–20. https://doi.org/10.1534/genetics.112.140145.

Erjavec, N., Larsson, L., Grantham, J., and Nyström, T. (2007). Accelerated aging and failure to segregate damaged proteins in Sir2 mutants can be suppressed by overproducing the protein aggregation-remodeling factor Hsp104p. Genes Dev. *21*, 2410–2421. https://doi.org/10.1101/gad.439307.

Ernst, R., Klemm, R., Schmitt, L., and Kuchler, K. (2005). Yeast ATP-binding cassette transporters: cellular cleaning pumps. Methods Enzymol. *400*, 460–484. https://doi.org/10.1016/S0076-6879(05)00026-1.

Fehrmann, S., Paoletti, C., Goulev, Y., Ungureanu, A., Aguilaniu, H., and Charvin, G. (2013). Aging yeast cells undergo a sharp entry into senescence unrelated to the loss of mitochondrial membrane potential. Cell Rep. *5*, 1589–1599. https://doi.org/10.1016/j.celrep.2013.11.013.

Fuller, G.G., Han, T., Freeberg, M.A., Moresco, J.J., Ghanbari Niaki, A., Roach, N.P., Yates, J.R., III, Myong, S., and Kim, J.K. (2020). RNA promotes phase separation of glycolysis enzymes into yeast G bodies in hypoxia. Elife *9*, e48480. https://doi.org/10.7554/eLife.48480.

Garcia, J.F., and Parker, R. (2015). MS2 coat proteins bound to yeast mRNAs block 5' to 3' degradation and trap mRNA decay products: implications for the localization of mRNAs by MS2-MCP system. RNA *21*, 1393–1395. https://doi.org/10.1261/rna.051797.115.

Garcia, J.F., and Parker, R. (2016). Ubiquitous accumulation of 3' mRNA decay fragments in Saccharomyces cerevisiae mRNAs with chromosomally integrated MS2 arrays. RNA *22*, 657–659. https://doi.org/10.1261/rna.056325.116.

Goulev, Y., Morlot, S., Matifas, A., Huang, B., Molin, M., Toledano, M.B., and Charvin, G. (2017). Nonlinear feedback drives homeostatic plasticity in H2O2 stress response. Elife *6*, e23971. https://doi.org/10.7554/eLife.23971.

Guet, D., Burns, L.T., Maji, S., Boulanger, J., Hersen, P., Wente, S.R., Salamero, J., and Dargemont, C. (2015). Combining Spinach-tagged RNA and gene localization to image gene expression in live yeast. Nat. Commun. *6*, 8882. https://doi.org/10.1038/ncomms9882.

Haber, J.E. (2012). Mating-type genes and MAT switching in Saccharomyces cerevisiae. Genetics *191*, 33–64. https://doi.org/10.1534/genetics.111.134577.

Haimovich, G., Zabezhinsky, D., Haas, B., Slobodin, B., Purushothaman, P., Fan, L., Levin, J.Z., Nusbaum, C., and Gerst, J.E. (2016). Use of the MS2 aptamer and coat protein for RNA localization in yeast: a response to "MS2 coat proteins bound to yeast mRNAs block 5' to 3' degradation and trap mRNA decay products: implications for the localization of mRNAs by MS2-MCP system". RNA *22*, 660–666. https://doi.org/10.1261/rna.055095.115.

Heinrich, S., Sidler, C.L., Azzalin, C.M., and Weis, K. (2017). Stem-loop RNA labeling can affect nuclear and cytoplasmic mRNA processing. RNA *23*, 134–141. https://doi.org/10.1261/rna.057786.116.

Heym, R.G., and Niessing, D. (2012). Principles of mRNA transport in yeast. Cell. Mol. Life Sci. *69*, 1843–1853. https://doi.org/10.1007/s00018-011-0902-4.

Huh, W.-K., Falvo, J.V., Gerke, L.C., Carroll, A.S., Howson, R.W., Weissman, J.S., and O'Shea, E.K. (2003). Global analysis of protein localization in budding yeast. Nature *425*, 686–691. https://doi.org/10.1038/nature02026.

Jo, M.C., Liu, W., Gu, L., Dang, W., and Qin, L. (2015). High-throughput analysis of yeast replicative aging using a microfluidic system. Proc. Natl. Acad. Sci. USA *112*, 9364–9369. https://doi.org/10.1073/pnas.1510328112.

Krumlauf, R. (1991). Northern blot analysis of gene expression. Methods Mol. Biol. *7*, 307–323. https://doi.org/10.1385/0-89603-178-0:307.

Kukhtevich, I.V., Lohrberg, N., Padovani, F., Schneider, R., and Schmoller, K.M. (2020). Cell size sets the diameter of the budding yeast contractile ring. Nat. Commun. *11*, 2952. https://doi.org/10.1038/s41467-020-16764-x.

Lengefeld, J., Cheng, C.-W., Maretich, P., Blair, M., Hagen, H., McReynolds, M.R., Sullivan, E., Majors, K., Roberts, C., Kang, J.H., et al. (2021). Cell size is a determinant of stem cell potential during aging. Sci. Adv. *7*, eabk0271. https://doi.org/10.1126/sciadv.abk0271.

Lenstra, T.L., and Larson, D.R. (2016). Single-molecule mRNA detection in live yeast. Curr. Protoc. Mol. Biol. *113*, 14.24.1–14.24.15. https://doi.org/10.1002/0471142727.mb1424s113.

Lerit, D.A., Smyth, J.T., and Rusan, N.M. (2013). Organelle asymmetry for proper fitness, function, and fate. Chromosome Res. *21*, 271–286. https://doi.org/10.1007/s10577-013-9350-3.

Li, Y., Jiang, Y., Paxman, J., O'Laughlin, R., Klepin, S., Zhu, Y., Pillus, L., Tsimring, L.S., Hasty, J., and Hao, N. (2020). A programmable fate decision landscape underlies single-cell aging in yeast. Science *369*, 325–329. https://doi.org/10.1126/science.aax9552.

Liu, B., Larsson, L., Caballero, A., Hao, X., Oling, D., Grantham, J., and Nyström, T. (2010). The polarisome is required for segregation and retrograde transport of protein aggregates. Cell *140*, 257–267. https://doi.org/10.1016/j.cell.2009.12.031.

Lui, J., Castelli, L.M., Pizzinga, M., Simpson, C.E., Hoyle, N.P., Bailey, K.L., Campbell, S.G., and Ashe, M.P. (2014). Granules harboring translationally active mRNAs provide a platform for P-body formation following stress. Cell Rep. *9*, 944–954. https://doi.org/10.1016/j.celrep.2014.09.040.

Miura, F., Kawaguchi, N., Yoshida, M., Uematsu, C., Kito, K., Sakaki, Y., and Ito, T. (2008). Absolute quantification of the budding yeast transcriptome by means of competitive PCR between genomic and complementary DNAs. BMC Genomics *9*, 574. https://doi.org/10.1186/1471-2164-9-574.

Moore, D.L., and Jessberger, S. (2017). Creating age asymmetry: consequences of inheriting damaged goods in mammalian cells. Trends Cell Biol. *27*, 82–92. https://doi.org/10.1016/j.tcb.2016.09.007.

Morales-Polanco, F., Bates, C., Lui, J., Casson, J., Solari, C.A., Pizzinga, M., Forte, G., Griffin, C., Garner, K.E.L., Burt, H.E., et al. (2021). Core Fermentation (CoFe) granules focus coordinated glycolytic mRNA localization and translation to fuel glucose fermentation. iScience *24*, 102069. https://doi.org/10.1016/j.isci.2021.102069.

Morlot, S., Song, J., Léger-Silvestre, I., Matifas, A., Gadal, O., and Charvin, G. (2019). Excessive rDNA transcription drives the disruption in nuclear homeostasis during entry into senescence in budding yeast. Cell Rep. *28*, 408–422.e4. https://doi.org/10.1016/j.celrep.2019.06.032.

Mortimer, R.K., and Johnston, J.R. (1959). Life span of individual yeast cells. Nature *183*, 1751–1752. https://doi.org/10.1038/1831751a0.

Müller, M., Heuck, A., and Niessing, D. (2007). Directional mRNA transport in eukaryotes: lessons from yeast. Cell. Mol. Life Sci. *64*, 171–180. https://doi.org/10.1007/s00018-006-6286-1.

Nadal-Ribelles, M., Islam, S., Wei, W., Latorre, P., Nguyen, M., de Nadal, E., Posas, F., and Steinmetz, L.M. (2019). Sensitive high-throughput single-cell RNA-seq reveals within-clonal transcript correlations in yeast populations. Nat. Microbiol. *4*, 683–692. https://doi.org/10.1038/s41564-018-0346-9.

Neurohr, G.E., Terry, R.L., Lengefeld, J., Bonney, M., Brittingham, G.P., Moretto, F., Miettinen, T.P., Vaites, L.P., Soares, L.M., Paulo, J.A., et al. (2019). Excessive cell growth causes cytoplasm dilution and contributes to senescence. Cell *176*, 1083–1097.e18. https://doi.org/10.1016/j.cell.2019.01.018.

Newman, J.R.S., Ghaemmaghami, S., Ihmels, J., Breslow, D.K., Noble, M., DeRisi, J.L., and Weissman, J.S. (2006). Single-cell proteomic analysis of S. cerevisiae reveals the architecture of biological noise. Nature *441*, 840–846. https://doi.org/10.1038/nature04785.

Ottoz, D.S.M., Rudolf, F., and Stelling, J. (2014). Inducible, tightly regulated and growth condition-independent transcription factor in Saccharomyces cerevisiae. Nucleic Acids Res. *42*, e130. https://doi.org/10.1093/nar/gku616.

Ozawa, T., Natori, Y., Sato, M., and Umezawa, Y. (2007). Imaging dynamics of endogenous mitochondrial RNA in single living cells. Nat. Methods *4*, 413–419. https://doi.org/10.1038/nmeth1030.

Padovani, F., Mairhörmann, B., Falter-Braun, P., Lengefeld, J., and Schmoller, K.M. (2022). Segmentation, tracking and cell cycle analysis of live-cell imaging data with Cell-ACDC. BMC Biol. *20*, 174. https://doi.org/10.1186/s12915-022-01372-6.

Paige, J.S., Wu, K.Y., and Jaffrey, S.R. (2011). RNA mimics of green fluorescent protein. Science *333*, 642–646. https://doi.org/10.1126/science.1207339.

Panchapakesan, S.S.S., Ferguson, M.L., Hayden, E.J., Chen, X., Hoskins, A.A., and Unrau, P.J. (2017). Ribonucleoprotein purification and characterization using RNA Mango. RNA *23*, 1592–1599. https://doi.org/10.1261/rna.062166.117.

Schmoller, K.M., Turner, J.J., Kõivomägi, M., and Skotheim, J.M. (2015). Dilution of the cell cycle inhibitor Whi5 controls budding-yeast cell size. Nature *526*, 268–272. https://doi.org/10.1038/nature14908.

Seel, A., Padovani, F., Finster, A., Mayer, M., Bureik, D., Osman, C., Klecker, T., and Schmoller, K.M. (2022). Regulation with cell size ensures mitochondrial DNA homeostasis during cell growth. Preprint at bioRxiv. https://doi.org/10.1101/2021.12.03.471050.

Shcheprova, Z., Baldi, S., Frei, S.B., Gonnet, G., and Barral, Y. (2008). A mechanism for asymmetric segregation of age during yeast budding. Nature *454*, 728–734. https://doi.org/10.1038/nature07212.

Shlyakhtina, Y., Moran, K.L., and Portal, M.M. (2019). Asymmetric inheritance of cell fate determinants: focus on RNA. Noncoding RNA *5*, 38. https://doi.org/10.3390/ncrna5020038.

Song, W., Strack, R.L., Svensen, N., and Jaffrey, S.R. (2014). Plug-and-Play fluorophores extend the spectral properties of Spinach. J. Am. Chem. Soc. *136*, 1198–1201. https://doi.org/10.1021/ja410819x.

Spellman, P.T., Sherlock, G., Zhang, M.Q., Iyer, V.R., Anders, K., Eisen, M.B., Brown, P.O., Botstein, D., and Futcher, B. (1998). Comprehensive identification of cell cycle-regulated genes of the yeast Saccharomyces cerevisiae by microarray hybridization. Mol. Biol. Cell *9*, 3273–3297. https://doi.org/10.1091/mbc.9.12.3273.

Stahl, T., Hümmer, S., Ehrenfeuchter, N., Mittal, N., Fucile, G., and Spang, A. (2019). Asymmetric distribution of glucose transporter mRNA provides a growth advantage in yeast. EMBO J. *38*, e100373. https://doi.org/10.15252/embj.2018100373.

Swaffer, M.P., Kim, J., Chandler-Brown, D., Langhinrichs, M., Marinov, G.K., Greenleaf, W.J., Kundaje, A., Schmoller, K.M., and Skotheim, J.M. (2021). Transcriptional and chromatin-based partitioning mechanisms uncouple protein scaling from cell size. Mol. Cell *81*, 4861–4875.e7. https://doi.org/10.1016/j.molcel.2021.10.007.

Tutucci, E., Maekiniemi, A., Snoep, J.L., Seiler, M., van Rossum, K., van Niekerk, D.D., Savakis, P., Zarnack, K., and Singer, R.H. (2022). Cyclin CLB2 mRNA localization determines efficient protein synthesis to orchestrate bud growth and cell cycle progression. Preprint at bioRxiv. https://doi.org/10.1101/2022.03.01.481833.

Tutucci, E., Vera, M., Biswas, J., Garcia, J., Parker, R., and Singer, R.H. (2018). An improved MS2 system for accurate reporting of the mRNA life cycle. Nat. Methods *15*, 81–89. https://doi.org/10.1038/nmeth.4502.

Tyagi, S. (2007). Splitting or stacking fluorescent proteins to visualize mRNA in living cells. Nat. Methods *4*, 391–392. https://doi.org/10.1038/nmeth0507-391.

Tyagi, S. (2009). Imaging intracellular RNA distribution and dynamics in living cells. Nat. Methods *6*, 331–338. https://doi.org/10.1038/nmeth.1321.

Unal, E., Kinde, B., and Amon, A. (2011). Gametogenesis eliminates age-induced cellular damage and resets life span in yeast. Science *332*, 1554–1557. https://doi.org/10.1126/science.1204349.

Urbanek, M.O., Galka-Marciniak, P., Olejniczak, M., and Krzyzosiak, W.J. (2014). RNA imaging in living cells - methods and applications. RNA Biol. *11*, 1083–1095. https://doi.org/10.4161/rna.35506.

Wierman, M.B., and Smith, J.S. (2014). Yeast sirtuins and the regulation of aging. FEMS Yeast Res. *14*, 73–88. https://doi.org/10.1111/1567-1364.12115.

Xu, Z., Wei, W., Gagneur, J., Perocchi, F., Clauder-Münster, S., Camblong, J., Guffanti, E., Stutz, F., Huber, W., and Steinmetz, L.M. (2009). Bidirectional promoters generate pervasive transcription in yeast. Nature *457*, 1033–1037. https://doi.org/10.1038/nature07728.

Youk, H., Raj, A., and van Oudenaarden, A. (2010). Imaging single mRNA molecules in yeast. Methods Enzymol. *470*, 429–446. https://doi.org/10.1016/S0076-6879(10)70017-3.

Zakian, V.A., Brewer, B.J., and Fangman, W.L. (1979). Replication of each copy of the yeast 2 micron DNA plasmid occurs during the S phase. Cell *17*, 923–934. https://doi.org/10.1016/0092-8674(79)90332-5.

Zhang, J., Fei, J., Leslie, B.J., Han, K.Y., Kuhlman, T.E., and Ha, T. (2015). Tandem Spinach array for mRNA imaging in living bacterial cells. Sci. Rep. *5*, 17295. https://doi.org/10.1038/srep17295.

Zion, E.H., Chandrasekhara, C., and Chen, X. (2020). Asymmetric inheritance of epigenetic states in asymmetrically dividing stem cells. Curr. Opin. Cell Biol. *67*, 27–36. https://doi.org/10.1016/j.ceb.2020.08.003.

STAR★METHODS

KEY RESOURCES TABLE

REAGENT or RESOURCE	SOURCE	IDENTIFIER
Chemicals, peptides, and recombinant proteins		
DFHBI-1T	TOCRIS, UK	Cat. No. 5610
TO1-B	Laboratory of Peter Unrau	Published in https://doi.org/10.1021/cb500499x
BI	Lucerna, USA	Cat. No. 600-1mg
Photoresist SU-8 2025	MicroChem, USA	Product No. Y111069
Photoresist SU-8 2002	MicroChem, USA	Product No. Y111029
Polydimethylsiloxane kit Sylgard 184	Dow Corning, USA	Material Number 1673921
Drop-out Mix Synthetic minus Histidine, Leucine, Tryptophan, Uracil w/o yeast Nitrogen Base	US Biological	L14110761
Drop-out-mix complete w/o yeast nitrogen base	US Biological	Cat #D9515
Difco Yeast Nitrogen Base w/o Amino Acids	Becton-Dickinson	Ref 291940
L-Leucine	Sigma	L8000-50G
L-Histidine	Sigma	53319–100G
D-(+)-Glucose	Sigma	G8270-100G
Ethanol	Sigma-Aldrich	1.00983.1000
Glycerol	Sigma-Aldrich	G9012-1L
Stellaris® RNA FISH Hybridization Buffer	Biosearch Technologies, UK	SMF-HB1-10
Stellaris® RNA FISH Wash Buffer A	Biosearch Technologies, UK	SMF-WA1-60
Stellaris® RNA FISH Wash Buffer B	Biosearch Technologies, UK	SMF-WB1-20
Experimental models: Organisms/strains		
Saccharomyces cerevisiae. See Table S1 for details on strains	N/A	N/A
Oligonucleotides		
Stellaris® ENO2 smFISH probes	Biosearch Technologies, UK	N/A
Stellaris® SUT509 smFISH probes	Biosearch Technologies, UK	N/A
Recombinant DNA		
pRS406	Addgene, USA	U03446
pUG27 plasmid	EUROSCARF, Germany	P30115
pSH47 plasmid	EUROSCARF, Germany	P30119
Software and algorithms		
PhyloCell	Laboratory of Gilles Charvin	https://github.com/gcharvin
Autotrack	Laboratory of Gilles Charvin	https://github.com/gcharvin
MATLAB	MathWorks	Versions R2018b and R2021a
Cell ACDC	Laboratory of Kurt M. Schmoller	https://github.com/SchmollerLab/Cell_ACDC
Python	Python Software Foundation, USA	Python 3.8.5
Nikon NIS Elements	Nikon, Japan	Version 4.51.c1 and 5.02.01
ZEN (Zeiss software)	Zeiss, Germany	ZEN 2.6, blue edition

(Continued on next page)

Continued

REAGENT or RESOURCE	SOURCE	IDENTIFIER
Fiji (ImageJ)	Wayne Rasband National Institutes of Health, USA	Version 1.53 c
Other		
24 × 50 mm #1.5 glass coverslip	Knittel Glass, Germany	Cat# VD12450Y1A.01
1 mm biopsy puncher	Integra Miltex, USA	Cat# 33–31AA-P/25
Tygon tubing 0.02 inch ID × 0.060 inch OD	Cole-Parmer, Germany	Cat# GZ-06419-01
18 gauge 0.5 inch bent 90° blunt needle	Techcon, USA	Cat# TE718050B90PK
Microfluidic flow controller	Elveflow, France	Cat# OB1 MK3+
Microfluidic flow sensor	Elveflow, France	Cat# MFS 3
Port selector valve	Idex, USA	Cat# MXX778-605
Objective heater	Okolab, Italy	N/A
Heating chip holder	custom-built	N/A
Epifluorescence microscope	Nikon, Japan	Cat# Eclipse Ti-E
100× Objective	Nikon, Japan	Cat# plan-apo λ 100×/1.45 NA Ph3 oil immersion
Light engine	Lumencor, USA	Cat# SPECTRA X
EMCCD camera	Andor, UK	Cat# iXon Ultra 888
Confocal microscope	Zeiss, Germany	LSM 800
CCD camera	Zeiss, Germany	Axiocam 506 mono

RESOURCE AVAILABILITY

Lead contact

Further information and requests for resources and reagents should be directed to the lead contact, Robert Schneider (robert.schneider@helmholtz-muenchen.de).

Materials availability

This study did not generate any unique reagents.

Data and code availability

- Datasets used for figures in the manuscript are included in SI (Data S1).
- This paper does not report any original code.
- Any additional information required to reanalyze the data reported in this paper is available from the lead contact upon request.

EXPERIMENTAL MODEL AND SUBJECT DETAILS

All *S. cerevisiae* strains used in this study are based on Y7092 (wild-type), which was also used as an autofluorescence control. See Table S1 for additional information on the strains. Strains are available from the lead contact upon request.

METHOD DETAILS

Strain construction

S. cerevisiae strains were constructed using standard lithium acetate transformation and additional information on them is available in Table S1. Where specified, we used *NAB2NLS-2xmCHERRY-URA3* for visualization of nuclei, and *ENO2-mCHERRY*, *ENO2-sfGFP* and *SHE2-mCHERRY* for assessing Eno2 and She2 protein levels. Strains with inducible Whi5 are constructed in analogy to strains established in (Kukhtevich et al., 2020). Briefly, Whi5 is an inhibitor of the transcription factor SBF, which controls a large set of genes required for S-phase entry (Figure 7A) (de Bruin et al., 2004; Costanzo et al., 2004). By controlling cell cycle entry in a size-dependent manner (Schmoller et al., 2015), Whi5 acts as a cell size regulator. Thus, by tuning Whi5 concentration using an artificial controllable promoter (Ottoz et al., 2014), we can strongly alter steady-state cell size without major effects on population doubling time (Kukhtevich et al., 2020; Claude et al., 2021). Strains are available upon request.

Aptamer-based tagging strategy

We used the diSpinach aptamer (Figure S1A, Table S2) and the previously published Mango III aptamer (Autour et al., 2018). The diSpinach aptamer combines two repeats of the iSpinach aptamer (Autour et al., 2016), with the loop of the first repeat replaced by the second repeat to improve the folding efficiency (Figure S1A). For all mRNAs, we inserted the tag directly after the stop codon, while SUT509 ncRNA was tagged directly after the corresponding sequence. For *MANGO III* repeats we used 'AAAA' as a universal spacer; for *diSPINACH* repeats 20 random base pairs, except a middle 40 base pair spacer of 16xdiSpinach repeats, which was used due to cloning restrictions (Table S2). The 20 base pair spacers were checked using *IPknot* to avoid the formation of secondary structures. We inserted 1x, 2x, 4x, 8x and 16x repeats of *diSPINACH* and 12x repeats of *MANGO III* to tag *ACT1pr-mCHERRY* (1000 base pairs upstream of the start codon were used as the promoter) on a 2μOri expression plasmids with *URA3* as selection marker. Eight repeats of *diSPINACH* were used to tag *SUT509pr-SUT509* (500 base pairs upstream of the start codon were used as a promoter) on a 2μOri expression plasmid. A plasmid carrying *HHO1pr-mCHERRY-8xdiSPINACH* (1000 base pairs upstream of the start codon were used as the promoter) and *URA3* as a selection marker was assembled and integrated into the *URA3* locus. Plasmids carrying diSpinach-tagged constructs are based on pRS406. For high copy plasmids, a 2μOri was inserted at the ZraI site. For endogenous tagging of RNAs, we constructed a plasmid based on the pUG27 backbone with *LEU2* as a selection marker, replacing *HIS5* between two *LOXP* sites and followed by eight repeats of *diSPINACH*. After successful tagging of endogenous RNAs with *LOXP-LEU2-LOXP-8xdiSPINACH*, *LEU2* was removed by Cre-Lox recombination as previously described (Guet et al., 2015). In brief, Cre-recombinase was expressed from the pSH47 plasmid to promote the recombination.

Growth conditions

Prior to experiments, cells were grown overnight at 30°C in liquid synthetic complete medium with 2% dextrose as a carbon source (SCD). Strains carrying 2μOri expression plasmids with *URA3* as a selection marker were instead grown in liquid synthetic complete medium without uracil and with 2% dextrose. Saturated cultures were diluted in SCD and grown for 4–5 h to reach log phase (OD ~0.1–0.2) before starting microscopy experiments. Strains with inducible Whi5 were either not supplemented or additionally supplemented with one 400 nM dose of β-estradiol and grown over-night to achieve a wide distribution of accessible cell sizes. Note that we found that strains based on Y7092 require a significantly higher concentration of β-estradiol (400 nM) to induce a ~2 fold change in cell size compared to what we found for W303-based strains (Kukhtevich et al., 2020).

For the experiments described in Figures S2A, S2B, 50 μM DFHBI-1T (TOCRIS, Cat. No. 5610) or 1.25 or 12.5 μm TO1-B (kindly provided by Peter Unrau) was added to the cell culture 40 min prior to imaging in the well-device described below. For all time-lapse experiments using microfluidic devices, SCD medium with 50 μM DFHBI-1T was used (Figures 1, 2, 3, 4, 5, 6, 7 and S1B, S3, S4A, S4B, S4C, S4F, S4G, S7), except for a fluorophore washout experiment (Figures 6A–6C), for which SCD without DFHBI-1T was additionally used, and glucose withdrawal experiment (Figure S6D), for which SC (no glucose) with 50 μM DFHBI-1T was additionally used. We also tested 50 μM BI (Lucerna, Cat. No. 600-1mg) for imaging but 50 μM DFHBI-1T clearly performed better (Figure S2C).

Microfluidic devices

To acquire live single-cell data over a long period of time, we developed a custom-made microfluidics device that allows isolating cells in a dedicated region of interest, limiting colony growth to the XY-plane. The device (Figure 1A) includes eight separate cell culture chambers with a controllable medium exchange that enables imaging of up to eight strains simultaneously. The design can be provided upon request.

The microfluidic device was fabricated by means of standard soft lithography. Briefly, by using photolithography a master mold for replication of the device design in polydimethylsiloxane (PDMS) was fabricated from SU-8 photoresist (MicroChem, USA) spin-coated on a 3″ Si wafer. The master mold was then filled with a 10:1 mixture of the base to curing agent of PDMS kit Sylgard 184 (Dow Corning, USA) and left at 60°C for 4 h to crosslink the PDMS. After crosslinking, the PDMS replica was cut and peeled off from the master mold, and necessary inlets and outlets for tubing connections were made using a 1 mm puncher. Next, the replica was sealed with a coverslip after both were treated in O₂ plasma.

To test that our device does not affect cell growth, we compared doubling times of wild-type cells growing in SCD in liquid cultures and within the microfluidic device. Importantly, under typical imaging conditions, cell growth was not affected, and in both cases, we observed doubling times of approximately 80 min at 30°C.

The microfluidic device introduced here could be adapted for high-throughput applications and applied to other light-up aptamers (Bouhedda et al., 2018; Paige et al., 2011; Autour et al., 2016, 2018; Dolgosheina et al., 2014; Song et al., 2014; Chen et al., 2019).

For aging experiments, we used a microfluidic device designed to study aging in budding yeast (Morlot et al., 2019; Goulev et al., 2017). This device was fabricated by means of standard soft lithography as described above.

Well-device

To take still images of different strains (Figures S2A-S2C), we used a custom-made well-device made of PDMS and a coverslip. This device consists of eight separate wells, which can hold up to 100 μL of cell culture and can be sealed from the top with an additional coverslip. This device allows measuring live cells using high magnification oil immersion objectives, while preventing the culture from evaporation.

Live-cell microscopy

For live-cell microscopy using the well-device (Figures S2A-S2C), 80 μL of each cell culture were transferred into different wells. Then, the wells were sealed with a coverslip to prevent evaporation. Temperature control was achieved by setting a custom-made microscope incubator to 30°C.

Live-cell time-lapse experiments (Figures 1, 2, 3, 4B, 4C, 5, 7B, 7C and S1B, S3, S4A,S4B,S4C,S4F,S4G, S6A-S6F) were performed using the custom-made microfluidic device described above. Different strains were separately loaded in different chambers of the device. Constant medium flow at 20 μL/min was applied, enabling imaging of a colony growing over approximately 6 generations (10 h). For a fluorophore washout experiment, cells were grown for 3 h in SCD with the fluorophore and then for 7 h in SCD without fluorophore supplement (Figure S6A-S6C). For a glucose withdrawal experiment, cells were grown for 3 h in SCD with the fluorophore and then for 7 h in SC (no glucose) with the fluorophore supplement (Figure S6D). In the case of aging experiments (Figures 6B–6E, 7B-7D, and S7), we used an aging device described in (Morlot et al., 2019; Goulev et al., 2017), applied a constant medium flow at 10 μL/min, and performed imaging for up to ∼28 generations (up to 72 h). Temperature control was achieved by setting both a custom-made heatable insertion and an objective heater to 30°C.

A Nikon Eclipse Ti-E with SPECTRA X light engine illumination and an Andor iXon Ultra 888 camera were used for epifluorescence microscopy. A plan-apo λ 100x/1.45NA Ph3 oil immersion objective was used to take phase contrast and fluorescence images. diSpinach-related fluorescence was imaged by exposure for 300 ms, illuminating with the SPECTRA X engine at 480 nm and 19 mW power. Mango III-related fluorescence was imaged by exposure for 400 ms, illuminating with the SPECTRA X engine at 504 nm and 62 mW power. mCherry fluorescence was imaged by exposure for 200 ms, illuminating with the SPECTRA X engine at 556 nm and 13 mW power, except for endogenously integrated *HHO1pr-mCHERRY-8xdiSPINACH* and the corresponding autofluorescence experiments for which an exposure time of 400 ms and 26 mW power was used, as well as *ENO2-mCHERRY* and *SHE2-mCHERRY* strains for which exposure time of 200 ms and 26 mW power was used. sfGFP fluorescence was imaged by exposure for 300 ms, illuminating with SPECTRA X engine at 480 nm and 19 mW power. sfGFP fluorescence (emission at ∼ 510 nm), mCherry fluorescence (emission at ∼610 nm), DFHBI-1T fluorescence upon diSpinach binding (emission at ∼505 nm) and TO1-Biotin fluorescence upon Mango III binding (emission at ∼535 nm) were imaged using corresponding emission wavelengths filters.

FISH experiments for ENO2 RNA in SCD

For RNA fluorescence *in situ* hybridization (RNA FISH) we followed the protocols suggested in (Brown et al., 2018; Youk et al., 2010) and as described here. In brief, cells were grown in SCD medium overnight. The next day, cells were diluted in SCD medium for log-phase growth, and 27 mL of OD 0.5 culture was fixed with 3 mL 37% formaldehyde for 45 min. Cells were washed twice with 10 mL cold FISH buffer A (1.2 M sorbitol, 0.1 M KHPO$_4$ (pH 7.5)) and resuspended in 1 mL FISH buffer B (FISH buffer A, 20 mM ribonucleoside vanadyl complex (VRC), 20 μM 2-mercaptoethanol). Cell walls were digested with 375 U lyticase at 30°C for ∼45 min until ∼90% of cells were spheroplasted. From then on, spheroplasts were centrifuged at 400 g to prevent bursting. Cells were washed twice with 1 mL cold FISH buffer B without 2-mercaptoethanol, resuspended in 1 mL 70% ethanol, and stored overnight at 4°C. The next day, cells were resuspended in 100 μL FISH buffer C (2x SSC (300 mM NaCl, 30 mM sodium citrate), 10% dextran sulfate, 1 mg/mL E. coli tRNA, 2 mM VRC, 20 ug/mL BSA, 10% formamide) with 125 nM probe and incubated at 30°C overnight in the dark. with the following modifications: we used custom Stellaris RNA FISH probes, which contained 48 oligos labeled with Quasar 670 to detect ENO2 RNAs (Biosearch Technologies). We note that due to high sequence similarity, we expect these probes to also visualize ENO1 RNAs, which is however much less abundant compared to ENO2 in cells grown in a glucose-containing medium (Nadal-Ribelles et al., 2019). The following day, 100 μL FISH buffer D (2x SSC, 10% formamide) was added to the sample. Cells were centrifuged and resuspended in 1 mL FISH buffer D and incubated at 30°C in the dark for 30 min. Cells were then washed again with FISH buffer D (without incubation), resuspended in FISH buffer E (1 mL PBS with 25 ng/mL DAPI), and incubated at 30°C in the dark for 30 min. Cells were resuspended in a drop of ProLong Gold (Life Technologies) and mounted on a microscope slide with an 18 × 18 mm square #1 coverglass. The slides were stored overnight at room temperature in the dark. Finally, the coverslips were sealed with nail polish before imaging.

To image FISH samples we used the same microscopy setup as described in the "live-cell microscopy" section above except for different fluorescence imaging settings (Figure S5A). DAPI related fluorescence was imaged by exposure for 50 ms, illuminating with the SPECTRA X engine at 387 nm and 118 mW power. mCherry fluorescence was imaged by exposure for 100 ms, illuminating with the SPECTRA X engine at 556 nm and 26 mW power. FISH probes related fluorescence was imaged by exposure for 400 ms, illuminating with the SPECTRA X engine at 635 nm and 139 mW power. DAPI (emission ∼461 nm), mCherry (emission ∼610 nm) and FISH probe fluorescence (emission ∼670 nm) were imaged using corresponding emission wavelength filters.

FISH experiments for ENO2 RNA in SCGE and SUT509 in SCD

FISH experiments for *ENO2* in liquid synthetic complete medium with 2% glycerol and 1% ethanol (SCGE) and for *SUT509* in SCD medium were performed according to the Stellaris® RNA smFISH Protocol for *S. cerevisiae*, available online at www.biosearchtech.com/stellarisprotocols. For *ENO2*, the same custom Stellaris FISH probes were used as described for Figure S5F. We note that due to high sequence similarity, we expect these probes to also visualize the paralog *ENO1*. For *SUT509*, custom Stellaris FISH probes containing 40 oligos were used (Figure S4D). Each oligo was 20 nucleotides long and labeled with the

Quasar® - 570 fluorophore (Biosearch Technologies). Cells were inoculated in 5 mL of SCD or SCGE medium and incubated for at least 5 h at 30°C under shaking conditions (250 rpm). These cultures were then diluted to 50 mL and grown overnight to reach ODs of around 0.1 the next morning. DHFBI-1T was added to the cultures at a concentration of 50 μM and the cells were allowed to grow in media with DHFBI-1T for at least 2 h. Exponential phase cells were fixed at ODs 0.2–0.4 for SCD cultures and ODs 0.1–0.3 for SCGE cultures by addition of 5 mL of 37% formaldehyde to 45 mL of cell culture (final concentration 3.7%) and incubation at room temperature for 45 minutes. Fixed cells were washed twice with ice-cold fixation buffer (1.2 M sorbitol (Sigma-Aldrich), 0.1 M K2HPO4 (Sigma-Aldrich), pH 7.5), and were resuspended in 1 mL fixation buffer containing 6.25 μg zymolyase (Biomol). Cells were incubated for 55 min at 30°C for cell wall digestion. Following cell wall digestion, the spheroplasts were only centrifuged at 400g to prevent cell bursting. The digested cells were washed twice with ice-cold fixation buffer, resuspended in 70% EtOH and stored overnight at 4°C. Depending on the size of the cell pellet, 300–500 μL of digested cells were centrifuged and resuspended in 100 μL hybridization buffer (Stellaris® RNA FISH Hybridization Buffer (Biosearch Technologies) with 10% v/v formamide (VWR International)) containing a final Stellaris® FISH probe concentration of 125 nM. The cells were incubated overnight with the probe at 30°C in the dark. The following day, cells were first treated with 100 μL wash buffer A (Stellaris® RNA FISH 1X wash buffer A (Biosearch Technologies) with 10% v/v formamide), centrifuged and then incubated in 1 mL wash buffer A at 30°C for 30 min. Next, the cells were centrifuged and resuspended in 1 mL of a DAPI solution (5 ng/mL DAPI in wash buffer A). After incubation in the DAPI solution at 30°C for 30 min to stain the nuclear DNA, the cells were washed with Stellaris® RNA FISH wash buffer B by shaking at 500 rpm for 12 min in the Eppendorf®|VWR ThermoMixer™ C. Cells were centrifuged and resuspended in a drop of ProLong Gold Antifade Mountant (Invitrogen) before being mounted onto glass microscopy slides (Epredia™, SuperFrost Plus, 25 × 75 × 1 mm) using cover glasses (Carl Roth GmbH, High Precision Microscope Cover Glasses, 18 × 18 mm No. 1.5H). Each experiment consisted of at least two biological replicates and multiple images were acquired for each biological replicate.

The slides were imaged on a Zeiss LSM 800 microscope with an additional epifluorescence setup using a 63x/1.4NA oil immersion objective and a Zeiss Axiocam 506 camera. Epifluorescence stacks composed of 25 z-slices (0.24 μm step size) were acquired to cover the entire depth of cells. ENO2 FISH probes labeled with Quasar® - 670 fluorophore were imaged using the Colibri 630 LED module at 50% power and an exposure time of 400 ms. SUT509 FISH probes labeled with Quasar® - 570 fluorophore were imaged using the Colibri 511 LED module at 50% power and an exposure time of 5 s. DAPI signal was imaged using the Colibri 385 LED module at 30% power and an exposure time of 130 ms. Bright-field images were acquired using the TL Lamp at an intensity of 6% for an exposure time of 100 ms.

Impact of aptamer-based tagging on RNA

To assess how tagging with *8xdiSPINACH* impacts transcript concentrations we checked how it affects ENO2 RNA levels by analyzing our quantitative FISH data for ENO2 RNA (see description above, Figures S5A-S5C). This revealed ∼40% of ENO2 RNA in *ENO2-8xdiSPINACH* cells compared to wild-type cells, suggesting that the diSpinach aptamer may have a moderate effect on mRNA abundance (Figure S5B). We wish to emphasize that our FISH analyses confirm that the asymmetric distribution is not due to 8xdiSpinach tagging of the ENO2 RNA, since tagging does not affect the mother-daughter distribution (Figure S5C). Notably, the reduced levels of ENO2 RNA seem to not majorly impair cell viability and growth, consistent with the fact that even *eno2Δ* cells are viable and have no strong phenotype on glucose media (Entelis et al., 2006).

Northern blot

Northern blot analysis for *ACT1pr-mCHERRY-0/1/2/4/8xdiSPINACH* expressed from 2 μOri (Figures S1C, S1D) and endogenously expressed *ENO2 and ENO2-8xdiSPINACH* (Figures S5D, S5E) was carried out as described in (Krumlauf, 1991). In brief, equal amounts of total RNA (5μg per sample) were diluted in 10 μL TE buffer (final volume) and mixed with 1 μL 20x MOPS (0.1 M sodium acetate, 0.4M MOPS, and 20 mM EDTA), 10 μL 100% formamide, 3.5 μL 37% formaldehyde, 2 μL Blue Juice dye (0.1% xylene cyanol, 0.1% bromophenol blue, 1x MOPS, 50% glycerol). RNA was denatured at 60°C for 15 min, cooled on ice and loaded immediately on a 1% agarose gel containing 1x MOPS and ∼6.3% formaldehyde. The gel was run for 4h at 60V and then soaked in 50 mM NaOH, 0.1M NaCl for 20 min with gentle shaking. The gel was then neutralized by incubating in 0.1M Tris-HCl pH 7.6 for 20 min followed by incubation with 2x SSC (0.3M NaCl, 30mM sodium citrate) for 20 min with gentle shaking. RNA was then transferred onto a positive Nylon membrane (Amersham Hybond™-N, GE Healthcare) overnight by capillary transfer in 20x SSC buffer (3M NaCl, 0.3M sodium citrate). After blotting, the membrane was briefly rinsed with 6x SSC buffer and RNA crosslinked to the membrane by 254nm UV light with a total energy output of 2400J. The membrane was then placed between two sheets of 3MM Whatman paper and baked at 80°C for 60 min. For prehybridization, the membrane was incubated with hybridization buffer (50% formamide, 5x SSC, 1x Denhardt's reagent, 20 mM sodium phosphate buffer, pH 6.8, 100μg/mL sheared denatured Salmon sperm DNA, 1% SDS and 10% dextran sulfate) for 1h at 50°C. DNA probes (*mCHERRY*, *ENO2*, *diSPINACH*) for hybridization were generated from PCR products or synthesized oligonucleotides using the RadPrime DNA labeling system (Invitrogen) with incorporation of [γ−32P]dATP (Hartmann Analytik) according to the instructions of the manufacturer. Hybridization was done overnight at 50°C. The next day, the membrane was washed twice in 30–40 mL of 0.1x SSC, 0.5% SDS at 60°C for 20 min and exposed to phosphor-imaging screens. Images were acquired with the Typhoon FLA 7000 imaging system.

QUANTIFICATION AND STATISTICAL ANALYSIS

Cell segmentation
For experiments shown in Figures 1, 2, 3, 4, 5, 6, 7 and S1, S4A, S4B, S4C, S4F,S4G, S5A-S5C, S6, S7 cells were automatically or manually segmented based on phase-contrast images using the *Matlab*-based *Phylocell* software (Fehrmann et al., 2013). Results of automatic segmentation were visually inspected and manually corrected if necessary.

For FISH experiments shown in Figures S4D, S4E, S5F-S5H, cell segmentation, cell volume calculations, lineage annotations and cell-cycle stage assignments were performed using the Cell-ACDC (v1) toolkit available at https://github.com/SchmollerLab/Cell_ACDC (Padovani et al., 2022). More specifically, we used the YeaZ neural network option in Cell-ACDC for segmentation (Dietler et al., 2020).

Image processing
To minimize the effect of pixel-noise and background fluorescence, we first applied a 5x5 pixel-moving average filter on fluorescence images. We used this filter since a 5x5 pixel field is around the optical resolution of our microscope setup and therefore allowed us to remove pixel and camera noise and robustly identify a signal that is higher than "autofluorescence" in a strain without any fluorescent tag. Then for each image, we subtracted the background signal calculated as the median from two areas, 200x200 pixels (or equivalent) each, selected to not contain any cells (Figures 1A, S2E). The background signal subtraction was not applied for the data presented in Figures 6, 7 and S7.

Cell autofluorescence control
The wild-type strain (Y7092) without any genetic modifications was used as the autofluorescence control for all experiments except experiments that required the induction of Whi5 with β-estradiol. For these experiments, the Whi5-inducible stain constructed without any additional modifications in the Y7092 background was used. Here, autofluorescence refers to cellular autofluorescence as well as potential cell-dependent fluorescence of the fluorophores even in the absence of aptamers.

Quantification of the RNA and protein signals
To quantify the RNA signal, we further analyzed the images obtained after applying the moving average filter and background subtraction.

For the 'quantitative approach' used in Figures 2A–2C, 3A, 3C, 3E, 3G, 3H, 4B, 4C, 5, 6B-6E, 7B-7D, and S1E, S6B, S6C, S6E-S6H, S7A, S7C, S7D, S7F-S7J, S7L, we used a threshold defined as the median pixel intensity plus two standard deviations calculated from the autofluorescence control to distinguish RNA or protein signal from autofluorescence. To measure the strength of the RNA or protein signal, we then summed the intensity of all pixels within the cell contour with intensity above the threshold. If five pixels or less were above the threshold, the RNA or protein signal was set to zero.

For the alternative 'binary approach' used in Figures 2D, 3B, 3D, 3F, and S4C, we instead used a threshold defined as the median pixel intensity plus three standard deviations calculated from the autofluorescence control. We then classified a cell as "cell with RNA signal" if the pixel intensity of more than five pixels exceeded the threshold.

Signal normalization
For most genes, bigger cells contain higher numbers of RNA molecules than smaller cells. Correspondingly, for most genes, RNA concentration is more similar in small and big cells (Claude et al., 2021; Swaffer et al., 2021). It is also known that cell size is a major reason for intrinsic variability in transcript or protein content between cells (Newman et al., 2006). To correct for this intrinsic variability in the RNA, mCherry protein, She2-mCherry, Eno2-mCherry and Eno2-sfGFP signals caused by differences in cell sizes, we normalized the signal by the corresponding cell area (Figures 1D, 2A, 2C, 3A, 3C, 3E, 3G, 3H, 4B, 4C, 5, 6B-6E, 7B-7D, and S1B, S1E, S1F, S4B, S6B, S6C, S6E-S6H, S7A, S7C, S7D, S7F-S7J, S7L). We decided to use the cell area for normalization because all images were acquired only in one focal plane (in focus) during the time-lapse experiments and the localized character of the signal together with the analysis approach implies that the signal recorded will be dominated by in-focus contributions.

Of note, for Eno2-mCherry and Eno2-sfGFP (Figures S6E-S6H), given a mean bud/mother area ratio of approximately 0.6, normalizing by the cell volume rather than the cell area would result in a bud/mother signal ratio of approximately 1.2. We expect this number to be an upper estimate for the bud/mother protein signal ratio, and therefore conclude that Eno2 protein inheritance does not show pronounced asymmetry.

For a direct comparison of RNA and protein dynamics for an individual cell over 10 h (Figure 2B), we normalized the RNA and protein signals on the corresponding values of the first time points shown.

Correlation analysis
For data presented in Figures 2A, 2B, and S1B, S4F, S4G, S7C, S7F, S7L, we applied the "corrcoef" function in MATLAB to calculate Pearson correlation coefficients and corresponding p-values to test against the null hypothesis that there is no relationship between the observed variables.

Multi-variable linear regression

Multi-variable linear regressions were performed using the MATLAB function "glmfit". For each parameter, linear regression provides a coefficient and a corresponding p-value, which tests whether the coefficient is statistically significantly different from 0. If the coefficient is statistically significantly different from 0, it implies that the corresponding parameter adds predictive information to the model. In our case, we tested the following parameters against the daughter/mother ENO2 diSpinach RNA signal ratio: division/generation number, mother cell area, daughter cell geometry (length of cell major axis/length of cell major axis), and mother S-G2-M phase duration. We found that only division/generation number (p = 0.029) and mother cell area (p = 0.046) but not cell geometry (p = 0.795) or duration of mother S-G2-M phase (p = 0.132) are significantly predictive.

Testing different numbers of diSpinach repeats

To characterize the signal intensities of different numbers of diSpinach repeats, we compared the RNA (diSpinach) signal normalized by cell area with the corresponding protein (mCherry) signal normalized by cell area for all analyzed cells at all time points (Figure S1B). For Figure 1D, we calculated the mean RNA (diSpinach) signal for cells with mean protein (mCherry) signal within +/− 100 [a.u.] bins of 500, 1000, 2000, 4000, and 8000 [a.u.] (N<=746 cells for each bin). For this, mothers and buds were counted as separate cells starting from bud emergence.

8xdiSpinach effect on expression from 2 μOri plasmids

For quantification of expression levels of *ACT1pr-mCHERRY* untagged and tagged with 8xdiSpinach from 2 μOri plasmids shown in Figure S4B, we used the quantitative approach to calculate mean protein (mCherry) signals in analyzed cells. Then, we plotted the number of cells (frequency) against the mCherry signal for both plasmids: without any tag (N = 8982 cells), with the 8xdiSpinach tag (N = 7943 cells).

Endogenous tagging with diSpinach repeats

For the quantification of RNA levels of genomic transcripts, we pooled all data from time-lapse experiments and applied both the quantitative and binary approaches. We plotted the mean RNA (diSpinach) signal normalized by cell area (Figure 2C) and the fraction of cells with detectable RNA signal (Figure 2D) for all analyzed strains.

Cell cycle analysis

For cell cycle analyses shown in Figures 3A–3F and S4C, mothers and their buds were counted as one cell before cytokinesis. For each strain, we analyzed at least 100 cell cycles. All data were aligned by bud emergence, and we included a range from 21 min before bud emergence, corresponding to the median beginning of G1-phase, to 60 min after bud emergence, corresponding to the median time of cytokinesis. For the data shown in Figures 3A, 3C, 3E, 95% confidence intervals were determined from 50000 bootstrap samples.

Single-cell pedigree analysis

For pedigree analysis shown in Figures 3G and 3H, the plots represent an overlay of pedigree information with heatmaps of RNA (diSpinach) signal levels for single mother cells and all their progeny. Mothers and their buds were counted as one cell before cytokinesis, which is depicted as a vertical black line in the plots. Mother-daughter connections were established by visual inspection using phase-contrast images.

For correlation of related and unrelated cells shown in Figures S4F, S4G, we arranged cells in two groups for each test: related mothers and daughters, unrelated mothers and daughters, and a mixture of unrelated mother or daughter cells in both groups. Next, we calculated for each time point from cytokinesis to 81 min (the estimated median duration of the cell cycle) corresponding Pearson correlation coefficients and p-values.

Analysis of RNA transport from a mother into its bud and corresponding protein levels

For RNA transport analyses shown in Figures 4, 5, S1E, S1F and protein level analyses shown in Figures S6E-S6H, mothers and their buds were analyzed separately starting from bud emergence. For each strain, we collected data for at least 90 cell cycles. We limited our analysis only to time points from bud emergence to median cytokinesis time (+60 min). We used the quantitative approach to calculate the mean RNA signal or protein signal for the mother part and the bud (Figures 4B, 5A, 5C, and S1E, S6E, S6G). 95% confidence intervals were determined from 50000 bootstrap samples. To characterize how the RNA signal or protein signal in the bud changes relative to the mother signal, we calculated the corresponding ratios for all strains (Figures 4C, 5B, 5D, and S1F, S6F, S6H).

Analysis of fluorophore availability in cells during time-lapse experiments

For analysis of fluorophore availability during a washout experiment shown in Figure S6B, mothers and their buds (some of them become daughters during the experiment) were tracked separately (N = 14 track cells for both) starting from the media change time point until 60 min after it. In the case of the analysis shown in Figure S6C, 52 single cells born before the media change time point and crossing it during their lifespan were tracked. For both analyses, we used the quantitative approach to calculate the mean RNA signal.

Analysis of experiments relating to replicative aging and cell size

For the analysis of asymmetric RNA inheritance shown in Figures 6 and 7, mothers and their daughters were analyzed separately at mother cytokinesis, as well as daughters and granddaughters at daughter cytokinesis.

For aging experiments with wild-type cells (Figures 6B, 6C, 7B, 7C, and S7), we tracked 40 mother cells and all their daughters at different divisions (N = 646 divisions overall), as well as daughters (N = 551 cells of different generations) and all the corresponding granddaughters (N = 547 newly born cells) at the first divisions of daughter cells. For aging experiments with *she2Δ* cells (Figure 6D), *SHE2-mCHERRY* cells (Figure 6E), and *sir2Δ* cells (Figure 7D), we tracked 40, 41, and 50 mother cells and all their daughters at different divisions, respectively. We used the quantitative approach, but omitting the background subtraction step, to calculate the mean RNA (diSpinach) and She2-mCherry signals for mothers, daughters and granddaughters (only for wild-type). It was not feasible to apply background subtraction due to the design of the aging device (Morlot et al., 2019; Goulev et al., 2017). More specifically, the cavity-like structures and extensively dividing yeast cells inside and outside the cavities resulted in a completely blocked field of view without the possibility to fit 200x200 pixels areas to calculate the median background value.

For experiments with the Whi5-inducible strain (Figures 7B and 7C), we collected data for 289 young mothers and 289 newly born daughters at the first division of mother cells. We applied here the same analysis as for aging experiments to be able to correctly match the two types of experiments.

Whiskers on Figures 6B–6E, 7B-7D and S7B, S7C, S7E, S7K represent standard errors.

FISH data analysis for ENO2 RNA in SCGE/SUT509 in SCD

Cell masks obtained from segmentation were manually corrected in the Cell-ACDC GUI and the DAPI reference channel was used to assign mother-bud pairs and cell-cycle stages. Cells with nuclear signal and no bud were assigned to G1 phase. Cells with nuclear signal having a bud with no nuclear signal were assigned to S phase, but only if the ratio of bud volume to mother volume was less than or equal to 0.2. The remaining cells with nuclear signal having a bud with no nuclear signal were assigned to G2/M phase. Cells and corresponding buds with clearly dividing nuclei were also assigned to G2/M phase. Cells and corresponding buds with clearly separated nuclei were only assigned to G2/M if bright-field images showed that cytokinesis was still underway.

The cell segmentation masks and mother-bud annotations obtained from cell-ACDC were used in the analysis of FISH spots, for which we adapted a custom spot detection routine written in Python previously described in (Seel et al., 2022). Briefly, we first applied a 3D Gaussian filter with a small sigma (0.75 voxels) followed by a 'Difference of Gaussians' filter. This was followed by 3D local maxima detection (peaks) by the *peak_local_max* function from the *scikit-image* library. The signal peaks were then filtered, in this particular case, by the Yen thresholding algorithm. Next, the peaks were subjected to quality control tests and overlapping spots were discarded. Quality control was done as described in points 6 and 7 in (Seel et al., 2022), but replacing the mitochondrial network by background intensity defined as a cellular signal not classified as spots. Specifically, spots with a mean signal lower than the cellular background were discarded). The remaining peaks were counted as valid RNA spots. The number of RNA spots per cell was combined with cell volumes and cell-cycle stages obtained from Cell-ACDC to obtain the plots shown in Figures S4C and S5G, S5H. In the SUT509 FISH experiments, around 9% of the cells were saturated with signals of FISH probes and were therefore excluded from the analysis.